THESIS FOR THE DEGREE OF LICENTIATE OF PHILOSOPHY

Simulation of Electro-Optic Modulators by a Time-Domain Beam-Propagation Method

Elin Solberg

Department of Mathematical Sciences
Division of Mathematics
Chalmers University of Technology and University of Gothenburg
Gothenburg, Sweden 2015

Simulation of Electro-Optic Modulators by a Time-Domain Beam-Propagation Method
Elin Solberg

Department of Mathematical Sciences
Division of Mathematics
Chalmers University of Technology and University of Gothenburg
SE-412 96 Gothenburg
Sweden
Telephone +46 (0)31 772 1000

Fraunhofer-Chalmers Research Centre for Industrial Mathematics
Chalmers Science Park
SE-412 88 Gothenburg
Sweden
Telephone +46 (0)31 772 4257
Email elin.solberg@fcc.chalmers.se

Typeset with LaTeX.
Printed in Gothenburg, Sweden 2015

Abstract

Electro-optic modulators (EOMs) are components which convert electric signals to optical ones. They are needed, e.g., at the transmitter end of fiber-optic communication systems and in time-stretch analog-to-digital converters. The development of new EOM designs to handle electric signals with higher frequencies is driven by the demand for ever-increasing bandwidths in telecommunications. As the process of building prototypes is time-consuming and expensive, it is highly desirable to increase the use of numerical simulations in the design process.

The topic of this thesis is numerical methods for simulation of high-speed EOMs. Two main challenges arise in this context: first, the device is optically very large; a wave propagation problem must be solved over tens of thousands of wavelengths. Second, due to the high frequencies of the modulating signal, the problem must be solved in time domain, rather than in frequency domain, as is otherwise common for waveguiding problems. A suitable method for this type of problem is the time-domain beam-propagation method (TD-BPM), which is particularly efficient for propagation over long distances, occurring mainly along a specified direction. If further the geometry varies slowly along that direction, a simplified formulation, called the paraxial TD-BPM, has previously been employed. Based on an analysis of the equations, and comparison to the related analysis of (linear) optical fibers, a modified paraxial formulation is suggested in the current work. We show that the modification, while adding neither complexity nor computational effort to the method, increases its accuracy significantly, especially for short pulses.

The TD-BPM has previously been discretized using finite differences. In this work we derive a weak formulation and a novel discretization based on tensor product finite elements. By using finite elements, discontinuities in material parameters at material interfaces can be represented in an exact manner, which is not possible with finite differences. Furthermore, non-uniform meshes with higher resolution where the data varies rapidly can be readily used with finite elements, and function spaces can be chosen flexibly. Full-vector and scalar versions of the weak and discrete formulations are derived.

Numerical results are presented for the scalar TD-BPM. The implementation is validated against analytic data for the case of pulse propagation in a straight waveguide. In addition, the results are compared to those of the finite-difference time-domain method, and the TD-BPM is shown to have higher accuracy for short pulses (pulse widths $10 - 50\,\mathrm{fs}$), when the modified paraxial approximation, suggested in this work, is employed. Finally, as a proof-of-concept case, the method is applied to an electro-optic modulator with simplified geometry but realistic modulating signal.

Keywords: time-domain beam-propagation method, finite element method, tensor products, computational electromagnetics, photonics, electro-optic modulators

Acknowledgements

First of all, I would like to thank my supervisor Professor Stig Larsson at the Department of Mathematical Sciences and my co-supervisor Associate Professor Fredrik Edelvik at Fraunhofer-Chalmers Centre (FCC) for many constructive discussions, and for your encouragement and guidance throughout my work on this licentiate thesis. Special thanks go to my colleague Dr. Stefan Jakobsson, with whom I have had the opportunity to work on the OptoScope project. Thank you for the nice collaboration, for your patience with my many questions, and for inspiring me to be more creative and trust my intuition when facing new problems. I am also thankful to Anders Ålund at FCC for always being ready to help with technical matters. I further wish to thank all of my colleagues at FCC for contributing to an inspiring working environment.

Finally, I want to thank my family, and especially my husband Olov, for your constant support and love – I am so blessed to share life with you – and God, the Creator of all, for life.

This work was supported by the Fraunhofer Internal Programs under Grant No. MAVO 824720.

Elin Solberg
Gothenburg, March 2015

Contents

Abstract **i**

Acknowledgements **iii**

1 Introduction **1**
1.1 Project background 1
1.1.1 Electro-optic modulators 2
1.1.2 Electric signal propagation 6
1.2 Technical problem statement 7
1.3 Scope 7

2 Theory **9**
2.1 Mathematical problem statement 9
2.1.1 Derivation of wave equations 9
2.1.2 Time-dependent permittivity 11
2.1.3 Boundary conditions and initial values 13
2.2 Propagation in straight optical waveguides 14
2.2.1 Propagating modes 14
2.2.2 Pulse propagation and dispersion 17

3 Methods **23**
3.1 Preliminaries 25
3.1.1 BPM 25
3.1.2 Space- and time-resolving methods 25
3.2 Moving-time TD-BPM 26
3.2.1 Derivation of the scalar equation 27
3.2.2 Abstract formulation 30
3.2.3 Weak formulation 33
3.2.4 Discretization 37

4 Results **43**
4.1 Pulse broadening in straight slab waveguide 43
4.2 Electro-optic modulator 48

5 Conclusion **53**

Bibliography **55**

Chapter 1

Introduction

1.1 Project background

This work has been done at Fraunhofer-Chalmers Research Centre for Industrial Mathematics (FCC) as a part of the project "MaVo[1] OptoScope – Optische Technologien für die ultraschnelle Elektronik" (hereafter referred to as "the OptoScope project"), which is a joint effort of FCC and three Fraunhofer institutes in Germany, Fraunhofer Institute for Physical Measurement Techniques, Fraunhofer Institute for Applied Solid State Physics, and Fraunhofer Institute for Industrial Mathematics. The aim of the project is to develop measuring equipment – a signal generator and an oscilloscope – for non-periodic, high-frequency electrical signals with bandwidths up to 1 THz. Such equipment, which is the enabling technology for developing high-frequency electric devices, is currently not commercially available; at the outset of the OptoScope project in April 2012, the fastest available oscilloscopes measured non-periodic signals with bandwidths up to 33 GHz.

The strategy used to realize the THz oscilloscope is a time-stretch system [1], performing the following steps:

1. convert the high-frequency electric signal to an optical signal using an electro-optic modulator (EOM),
2. stretch the optical signal in time by propagation through a dispersive fiber,
3. convert the (time-stretched) signal back to the electric regime using a fast photodiode,
4. measure the signal with a conventional oscilloscope.

The time-stretch setup is shown schematically in Figure 1.1, with some additional steps. The EOM in step 1 takes as input the electric signal, denoted in the figure

[1] MaVo stands for "Marktorientierte strategische Vorlaufforschung", a type of projects funded by Fraunhofer-Gesellschaft.

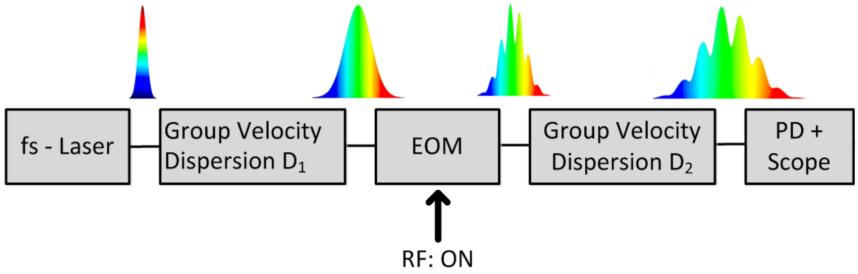

Figure 1.1: Schematic illustration of optical time-stretch system. Courtesy of Stefan Weber.

by "RF: ON"[2], and an optical pulse, which is amplitude modulated in the EOM by the electric signal. Step 2 corresponds to "Group Velocity Dispersion D_2" in the figure, and steps 3 and 4 are summarized in the box "PD + Scope". The figure also shows how the optical input to the EOM is generated: a broadband laser is used to generate an ultra-short optical pulse. Before entering the EOM the pulse is propagated through a dispersive fiber, which stretches it in time.

The EOM is a critical component of the system, and as EOMs capable of handling modulation frequencies up to 1 THz are not yet commercially available, the successful manufacturing of such a device has been one of the main aims and challenges of the OptoScope project. The role of FCC in the project has been to develop tools for the numerical simulation of EOMs. On the one hand, a model was needed to represent the EOM in system simulations, for optimization of the overall system performance. On the other hand, detailed simulations of the EOM were required, for optimization on the device level. Additionally, the latter model, using less assumptions, might be used to validate the former one. The present work concentrates on the detailed EOM simulations.

1.1.1 Electro-optic modulators

In this section, a very brief introduction to electro-optic modulators (EOMs) is given. The interested reader is referred to [2, 3] for more on this subject.

Optical waveguides

Before considering EOMs, we introduce one of their underlying structures: optical waveguides. Optical waveguides are guiding structures along which optical waves, i.e., electromagnetic waves in the visible or near-infrared frequency range, can propagate. Several types of optical waveguides exist; the most well-known is probably the optical fiber. The type of optical waveguides used in EOMs are planar dielectric waveguides, which consist of a core, in which the guided light is mainly confined, and a cladding surrounding the core. The core and cladding materials

[2]For historical reasons the electric signal is sometimes referred to as the radio frequency (RF) signal. In our application the frequencies may be well above radio frequencies.

are both dielectrics, characterized by the core having a higher refractive index than the cladding. A variety of designs of planar dielectric waveguides have been developed for different purposes, see, e.g., [2]. Figure 1.2 illustrates three different designs, which are of interest in this work: a rectangular guide, a rib guide and, a slab guide. The slab guide extends, theoretically, infinitely in the transverse hori-

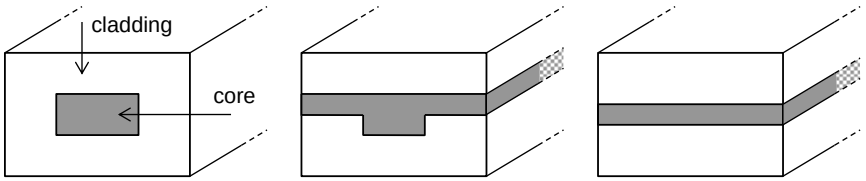

Figure 1.2: Schematic illustration of planar dielectric waveguides. Left: rectangular, center: rib, right: slab.

zontal direction. Since it confines light only in the vertical direction, it is not very useful in applications, however it is an important tool in the theoretical analysis of dielectric waveguides, as we will see later. The rib and immersed guides have both been suggested for use in the EOM developed in the OptoScope project.

In dielectric waveguides, light is confined in the core due to the refractive index difference between core and cladding. A different type of optical waveguide is the metallic (also called closed) waveguide, which consists of a dielectric core, enclosed by a metallic wall guiding the light. Such waveguides are not used in EOMs, but are, like the dielectric slab guide, interesting from a theoretical perspective.

A dielectric waveguide is characterized by the relative refractive index difference between core and cladding, defined as [4]

$$\Delta = \frac{n_1^2 - n_0^2}{2n_1^2} \approx \frac{n_1 - n_0}{n_1},$$

where n_1 and n_0 are the core and cladding refractive indices, respectively. Common waveguide materials have refractive indices above 1 (vacuum) and below 4 or 5. Typical values of Δ range between one and a few percent, but extremely high-index contrast waveguides with Δ in the range 10–40% also exist. Various core and cladding materials have been considered for the EOM in the OptoScope project, all with low contrasts, even below one percent.

Phase and amplitude modulation

The purpose of EOMs is to transfer the information carried by an electric signal to an optical one. There are several types of optical modulators, but here we consider only modulators based on the linear electro-optic (EO) effect, or Pockels effect. An EO material, i.e., a material exhibiting the EO effect, responds to an applied electric field by a slight shift in its refractive index. This in turn shifts the phase velocity of an optical wave propagating through the material. Based on this, a phase modulator can be constructed as schematically illustrated in Figure 1.3(a).

Electrodes are places on both sides of an optical waveguide, whose core is an EO material. One of the electrodes is grounded. A voltage applied to the other ("hot") electrode induces an electric field over the waveguide core, modulating its refractive index, which in turn modulates the phase of the optical field propagating through the waveguide. Note that the input of an EOM is thus twofold: a non-modulated, i.e., not (yet) information-carrying, optical pulse is fed into the optical waveguide, and an information-carrying electric signal is applied to the hot electrode. The output of interest is the modulated optical pulse. Amplitude modulation can

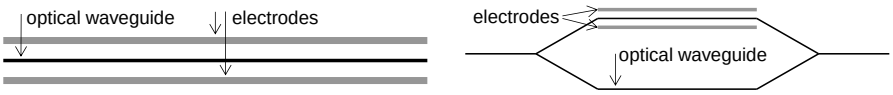

(a) Phase modulator (b) Amplitude modulator

Figure 1.3: Schematic illustration of modulators.

be achieved by using a Mach-Zehnder (MZ) interferometer structure, illustrated in Figure 1.3(b). Here the initial optical pulse splits equally between the two waveguide "arms", one of which is modulated by the electric signal. At the output end of the structure, the two pulses are recombined and interfere – constructively in the absence of modulation or destructively in the presence of modulation due to the phase difference between the non-modulated and the phase modulated pulse. Hence the recombined pulse is amplitude modulated. Alternatively, the electric field can be applied in opposite directions to the two MZ interferometer arms, resulting in the same phase shift at half the voltage. Such modulators are called push-pull modulators.

For slow electric signals, the time it takes the signal to propagate along the electrode is negligible compared to the time scale of the signal's temporal variations. Hence the voltage can at each instant be seen as constant along the device. Broadband modulators, however, like the one aimed at in the OptoScope project, treat electric signals with such fast temporal variations, that the traveling time of the signal along the electrode must be taken into account. One important design challenge of these so-called traveling-wave (TW) EOMs is to match the velocities of the co-propagating optical and electric signals.

Further design challenges are low electric and optical losses, and impedance matching of the electrodes, while competing design goals include increased bandwidth, decreased drive voltage and decreased device size. Concerning the latter, it should be noted, that the MZ interferometer geometry in Figure 1.3(b) is not according to scale. The distance between the arms is some tens or hundreds of micrometers, while their length is up to two centimeters. Also, the input/output regions are shorter than indicated, compared to the arms, and extend over maximally a few millimeters. The splitting and recombination of the waveguide arms may consist of Y junctions, as indicated in Figure 1.3(b), but may also be more complicated couplers, such as multimode interference couplers [2].

Electro-optic effect

The linear electro-optic effect, or Pockels effect, as described above, is the phenomenon by which the refractive index of a dielectric medium is slightly shifted in response to an applied electric field. The response time of the effect is very short, such that the response can be considered immediate (although, for modulation in the THz frequency range this approximation approaches its limit of validity for certain materials). We call the amount by which the refractive index changes due to the electro-optic effect, the refractive index shift, and denote it[3] by δ_n. It is anisotropic in general, however, the simple formula [3, Chapter 4]

$$\delta_n = -\frac{1}{2} n^3 r E$$

is highly accurate for many modulators, as long as the correct components are chosen for E and r. Here n is the refractive index of the medium without modulation, r is the electro-optic coefficient, a parameter quantifying the strength of the electro-optic effect in the material, and E is the modulating electric field. Hence δ_n is proportional to E, which is proportional to the modulating voltage. EOMs are typically operated at voltages producing a shift of order 10^{-4}, i.e., orders of magnitude smaller than the index contrast Δ.

We note here again, that only the waveguide core exhibits the EO effect. Further, due to the electrode configuration, see Section 1.1.2, the modulating electric field can be regarded as constant over the core cross section (which, by convention, lies in the $x - y$ plane). Hence we can write the spatial and temporal dependence of the shift in the EOM as

$$\delta_n(x, y, z; t) = -\frac{1}{2} n_{\text{core}}^3 \chi_{\text{core}}(x, y, z) r E(z; t), \tag{1.1}$$

where E is the modulating electric field, traveling along the electrodes, and χ_{core} is the characteristic function of the modulated core at z.

In the mathematical analysis it is often more natural to express the shift in terms of permittivity, denoted by ε. In lossless media $\varepsilon = n^2$, and for the shift we have

$$\varepsilon + \delta_\varepsilon = (n + \delta_n)^2 \approx n^2 + 2n\delta_n.$$

Hence the shift in permittivity is given by $\delta_\varepsilon \approx 2n_{\text{core}}\delta_n$.

Materials The most common material used for EOMs based on the linear electro-optic effect is lithium niobate ($LiNbO_3$), which has a relatively weak electro-optic effect ($n^3 r = 306\,\text{pm/V}$) compared to some other inorganic crystal materials, but has several advantages in terms of technology. It is, e.g., insensitive to changes in temperature, and waveguides can be fabricated by well established methods. In the OptoScope project, however, electro-optic polymers, which are an emerging

[3] In the literature, the shift is often denoted Δn. We prefer to use δ_n, to avoid confusion with Δ, the relative index difference between core and cladding in a waveguide.

class of electro-optic materials, are used for the modulator. Polymers with $n^3 r$ up to 1600 pm/V have been reported, and even though the fabrication technology is not as mature as for $LiNbO_3$, the materials are promising.

1.1.2 Electric signal propagation

Simulation of EOMs can be divided into two major sub-problems: (1) propagation of the modulating electric field, guided by the electrodes, and (2) propagation of the optical field guided by the optical waveguide, under influence of the modulating signal. The one-way coupling between the two problems is given by the refractive index shift due to modulation, according to (1.1), where E is the solution to problem (1), and δ_ε is part of the data of problem (2). While proper EOM simulation requires consideration of both parts, this work is restricted to the optical problem, (2), and assumes $\delta_\varepsilon = \delta_\varepsilon(x, y, z; t)$ to be given. For completeness we indicate in this section one approach to solve problem (1).

The transmission line used to guide the electric signal along the EOM arms is made up by a grounded electrode below the dielectrics (cladding and core) and a top electrode to which the modulating voltage is applied. This type of transmission line is known as a microstrip line, or stripline, and its cross section is illustrated in Figure 1.4. The transmission line is homogeneous in the longitudinal

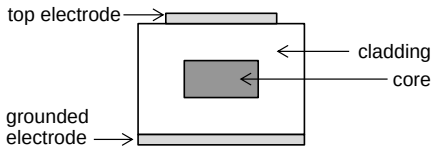

Figure 1.4: Cross section view of modulator arm.

direction, and – unlike the optical waveguide – time-independent. Hence, the propagation of the electric signal along the stripline can be computed in frequency domain, and transformed back to time domain by the fast Fourier transform. The frequency-dependent propagation characteristics of the transmission line can be computed approximately, using a finite element formulation of a quasi-TEM[4] approximation [5]. Here Poisson's equation,

$$\nabla \cdot (\varepsilon \nabla \Phi) = 0,$$

is solved for the scalar potential with homogeneous Dirichlet conditions on the ground plate and inhomogeneous Dirichlet conditions, corresponding to a normalized applied voltage, on the top electrode. Once this problem is solved, the intrinsic impedance η can be computed from the solution, and the electric and magnetic fields are given by

$$\mathbf{E} = -\nabla \Phi, \quad \mathbf{H} = -\frac{1}{\eta} \mathbf{E} \times \hat{z},$$

[4]TEM stands for transverse electromagnetic, meaning that both the electric and the magnetic fields have only transverse, and no longitudinal, components.

where the propagation direction of the transmission line is assumed to be aligned with the z axis. From the fields, the attenuation constants due to dielectric and conductor losses can be computed.

The main propagation characteristics to be anticipated are then attenuation along the transmission line, due to frequency-dependent losses, and possibly a velocity mismatch as compared to the group velocity of the optical signal.

1.2 Technical problem statement

The problem considered in this thesis is the numerical simulation of optical pulse propagation through traveling-wave electro-optic modulators (TW-EOMs). The pulses of interest are generated by letting ultra-short Gaussian pulses (pulse width $\sim$100 fs), with center wavelength $\lambda_0 = 1.55\,\mu$m, propagate through 1 km of dispersive fiber with group velocity dispersion parameter $\beta_2 \approx 50\,(\text{ps})^2/\text{km}$, such that the pulse width is stretched to a few hundred picoseconds. Based on the data given here, more specific characteristics of the stretched pulses are computed in Section 2.2.2, where pulse propagation and dispersion in optical fibers are discussed.

The electric input signal to the EOM, co-propagating with the optical pulse, may have a duration up to some tens of picoseconds and bandwidth up to 1 THz. The resulting high-frequency time-dependence of permittivity poses a numerical challenge, since it requires time domain analysis of the waveguide structure, rather than frequency domain analysis by, e.g., the well established beam-propagation method.

Typical geometries and materials used for TW-EOMs have been discussed in Section 1.1.1. In summary, the materials are dielectrics with slightly higher refractive index in the core layer than in the cladding layers, and in the active core, an electro-optic material is used, which responds to the modulating electric signal by a shift in its refractive index. This shift is orders of magnitude smaller than the index difference between core and cladding. Typical dimensions of the EOM are some tens of micrometers in the transverse directions, and one or a few centimeters in the longitudinal direction. The device is thus optically very large, tens of thousands of wavelengths long, which poses another numerical challenge concerning discretization of the spatial domain. As a rule of thumb when using, e.g., finite elements, wave problems should be resolved by at least ten elements per wavelength. Resolving the full device in space and time is thus computationally very expensive.

1.3 Scope

As stated above, EOM simulation can be divided into two major sub-problems, the electric propagation problem, and the optical propagation problem. These are coupled by the refractive index shift, δ_ε, due to modulation, which is computed from the solution to the former problem, and provides data for the latter. This work is restricted to the optical propagation problem, and $\delta_\varepsilon = \delta_\varepsilon(x, y, z; t)$ is

assumed given. Its dependence on time and transverse space is assumed to be separable at any z, as given by (1.1).

There are two main approaches for the optical propagation problem in an EOM: one in which the problem is subdivided into partial problems, accounting for different aspects of the full problem, and the other in which the full problem, in time and space, is considered at once. In the introduction to Chapter 3, these two approaches are more thoroughly described and compared. The aim of this work has been to follow the full-problem approach, and to develop a method tailored to be efficient and accurate for the specific application described in the previous section. More specifically, a time-domain beam-propagation method has been investigated, as an alternative to the standard finite-difference time-domain method, and a finite element-based version of it has been developed and implemented.

Once the propagation of the optical pulse in the EOM, under influence of a modulating signal, has been computed, characteristic parameters of the EOM can be obtained from the optical field data in a post-processing step. This is important when using simulations for design optimization, however, a discussion of such optimization is beyond the scope of this work, and post-processing will be done only for the purpose of validating the numerical results.

Two assumptions are made concerning the dielectric materials. First, we assume that non-linear effects are negligible over the length of the device. At low optical intensities, used for input pulses to the EOM, this assumption does not impose a serious restriction. Second, we consider only non-dispersive materials, i.e., materials in which the refractive index is independent of frequency, over the spectrum of the optical pulse. Considering the broad bandwidth of the pulse, this might be a more severe limitation. For better prediction of a real device's performance, a more realistic material model may be needed.

A final comment: the current text is written for mathematicians; it introduces the technical application – the EOM – and concepts from electromagnetic field theory starting from a basic level, but assumes some familiarity with mathematical concepts, especially those forming the basis of the finite element method. The relative emphasis on fundamentals, regarding application and mathematics, may well have been reversed, had the same work been written for (and by) electrical engineers.

Chapter 2

Theory

2.1 Mathematical problem statement

2.1.1 Derivation of wave equations

Maxwell's equations Optical waves are electromagnetic waves with frequencies in the visible or near-infrared spectrum. The most general mathematical model describing electromagnetic fields, and their dynamic interaction with media, is given by Maxwell's equations [6]

$$\nabla \times \mathbf{E} = -\partial_t \mathbf{B}, \tag{2.1a}$$
$$\nabla \times \mathbf{H} = \partial_t \mathbf{D} + \mathbf{J}, \tag{2.1b}$$
$$\nabla \cdot \mathbf{D} = \rho, \tag{2.1c}$$
$$\nabla \cdot \mathbf{B} = 0, \tag{2.1d}$$

where $\mathbf{E}$ is the electric field, $\mathbf{H}$ the magnetic field, $\mathbf{D}$ the electric flux density and $\mathbf{B}$ the magnetic flux density. Further, $\mathbf{J}$ is the current density and ρ is the charge density. In source-free media, such as dielectrics used in optical waveguide structures, $\mathbf{J} = 0$ and $\rho = 0$. The constitutive relation for the magnetic field and magnetic flux density is

$$\mathbf{B} = \mu_0 \mu \mathbf{H}, \tag{2.2}$$

where $\mu_0 \approx 1.257 \times 10^{-6}\,\mathrm{H/m}$ is the permeability of free space, and μ is the dimensionless relative permeability. The media of interest here are nonmagnetic with $\mu = 1$, however, we keep μ in the equations for generality.

We assume that the optical intensity is low enough, such that nonlinear effects are negligible over the length of the device (see [7] for a discussion of nonlinear length, i.e., the length scale over which nonlinear effects become important). Then the constitutive relation for the electric field and electric flux density is given by

$$\mathbf{D} = \varepsilon_0 \varepsilon \mathbf{E}, \tag{2.3}$$

where $\varepsilon_0 \approx 8.854 \times 10^{-12}\,\mathrm{F/m}$ is the permittivity of free space, and ε is the dimensionless relative permittivity. In anisotropic media ε is a tensor and in isotropic media it reduces to a scalar value. As stated in Section 1.3, we limit the discussion to non-dispersive media, i.e., media in which the permittivity is independent of frequency. Dispersive materials can be modeled in time domain by using the recursive convolution approach [8]. Materials used in optical waveguides are often specified in terms of their refractive index, n, which, in the isotropic case, relates to the relative permittivity as $\varepsilon = n^2$ [7].

Vector wave equations The vector wave equation for the electric field is derived from Maxwell's equations and the constitutive equations, by taking the curl of (2.1a) and using (2.1b), (2.2), and (2.3) to express the right hand side in $\mathbf{E}$ and eliminate $\mathbf{H}$. We get

$$\nabla \times (\mu^{-1}\nabla \times \mathbf{E}) = -\frac{1}{c^2}\partial_t^2(\varepsilon\mathbf{E}), \tag{2.4}$$

where $c = 1/\sqrt{\varepsilon_0\mu_0} = 299792458\,\mathrm{m/s}$ is the speed of light in free space.

In many electromagnetic applications, material properties are time independent, in particular, ε can be moved out of the time derivative. In an EOM, however, the permittivity is a function of time, due to the modulating signal, and it is shown in Section 2.1.2, that the approximation $\partial_t(\varepsilon\mathbf{E}) = \varepsilon\partial_t\mathbf{E}$ is not valid for the highest modulation frequencies of interest in the OptoScope project. For the EOM application we therefore keep the vector wave equation in the form stated above, rather than the more common form with right hand side $-\frac{\varepsilon}{c^2}\partial_t^2\mathbf{E}$.

Under assumption of time-independent permittivity, a similar wave equation for the magnetic field,

$$\nabla \times (\varepsilon^{-1}\nabla \times \mathbf{H}) = -\frac{\mu}{c^2}\partial_t^2\mathbf{H},$$

is derived by taking the curl of (2.1b) and using (2.1a) and the constitutive relations. However, here it is less clear how the corresponding wave equation should be formulated in the case of time-dependent ε. In the following we therefore restrict the discussion to the electric field formulation when considering EOMs with time-varying modulation.

Scalar wave equations For the derivation of the scalar wave equation we use (2.1c), with $\rho = 0$, in the form

$$0 = \nabla \cdot (\varepsilon\mathbf{E}) = \nabla\varepsilon \cdot \mathbf{E} + \varepsilon\nabla \cdot \mathbf{E}.$$

Using this and the vector identity

$$\nabla \times (\mu^{-1}\nabla\times) = -\nabla \cdot (\mu^{-1}\nabla) + \nabla(\mu^{-1}\nabla\,\cdot),$$

which holds for scalar permeability, we can write the left hand side of (2.4) as

$$\nabla \times (\mu^{-1}\nabla \times \mathbf{E}) = -(\nabla \cdot (\mu^{-1}\nabla))\mathbf{E} - \nabla(\mu^{-1}\varepsilon^{-1}(\nabla\varepsilon) \cdot \mathbf{E}).$$

The scalar approximation, which is valid when the spatial dependence of ε is weak, amounts to neglecting the second term of the right hand side. The scalar wave equation is then

$$\nabla \cdot (\mu^{-1} \nabla E) = \frac{1}{c^2} \partial_t^2 (\varepsilon E), \tag{2.5}$$

which holds for each of the three electric field components. Optical fields propagating in rectangular dielectric waveguides are polarized mainly along one of the transverse axes, and it is natural to solve the scalar wave equation for the corresponding dominating field component. The scalar approximation is typically used for waveguide analysis when the index contrast between core and cladding is small [4].

Helmholtz's equations In the case of time-harmonic electromagnetic fields we write

$$\mathbf{E}(x, y, z; t) = \mathrm{re}(\mathbf{E}(x, y, z) e^{j\omega t}),$$

and analogously for the magnetic field, where ω is the angular frequency. The quantities $\mathbf{E}(x, y, z)$ and $\mathbf{H}(x, y, z)$ are complex-valued, and referred to as phasors in electromagnetics. Inserting this into the wave equations is equivalent to substituting the differential operator $\frac{1}{c^2}\partial_t^2$ by multiplication with $-k_0^2$, where $k_0 = \omega/c$ is the wavenumber. This results in Helmholtz's equations for the corresponding phasor, e.g., the vector and scalar Helmholtz's equations for the electric field are, respectively

$$\nabla \times (\mu^{-1} \nabla \times \mathbf{E}) = \varepsilon k_0^2 \mathbf{E},$$

and

$$\nabla \cdot (\mu^{-1} \nabla E) = -\varepsilon k_0^2 E.$$

Due to the time-varying material properties in an EOM, resulting from the modulating signal, the analysis of such a device must be performed in the time domain. The numerical methods presented in Chapter 3 are therefore in most cases based on the wave equations. Yet, the propagation of optical waves in waveguides, in the absence of modulation, can be analyzed well in the frequency domain, using Helmholtz's equations, which form a basis for the mode analysis described in Section 2.2.1, as well as the beam-propagation method (BPM), described in Section 3.1.1.

2.1.2 Time-dependent permittivity

At any given point inside the active core of an EOM, the permittivity can be written

$$\varepsilon(t) = \varepsilon_\mathrm{c} + \delta_\varepsilon(t),$$

where ε_c is the constant permittivity of the core in the absence of modulation, and δ_ε is the time-dependent shift due to modulation. The shift δ_ε is proportional to

the voltage of the modulating signal, as described in Section 1.1.1. We then get, for the right hand side of the wave equation,

$$\partial_t^2(\varepsilon(t)\mathbf{E}) = \varepsilon_c \partial_t^2 \mathbf{E} + \partial_t^2(\delta_\varepsilon(t)\mathbf{E}),$$

where the first term in the right hand side governs the guiding of light in the waveguide when no modulating voltage is applied. The second term governs modulation, and is, in any realistic case, several orders of magnitude smaller in magnitude than the first term. The desired phase-modulating effect is obtained from this tiny shift by accumulation over the optically very long interaction distance, on the order of tens of thousands of wavelengths.

Having said this, we are now not interested in the absolute magnitude of the second term of the right hand side, nor in its magnitude relative to the first term. Rather we want to investigate whether or not the approximation

$$\partial_t^2(\delta_\varepsilon E) \approx \delta_\varepsilon \partial_t^2 E \tag{2.6}$$

is valid in our application, i.e., we consider the relative magnitudes of the terms that result from applying the product rule to the derivative on the left. We therefore write, at a given spatial point

$$\begin{aligned}\delta_\varepsilon(t) &= \delta_\varepsilon^{\max} f(t),\\ \mathbf{E}(t) &= \mathbf{E}^0 A(t) e^{j\omega_0 t},\end{aligned}$$

where $\delta_\varepsilon^{\max}$ and $\mathbf{E}^0$ are scaling factors, f is the normalized information-carrying modulating signal, and A is the normalized envelope of the optical pulse. We are then interested in the relative magnitudes of the terms in the right hand side of the expression

$$\begin{aligned}&\partial_t^2[f(t)A(t)e^{j\omega_0 t}]\\ &\qquad = \partial_t^2[f(t)]A(t)e^{j\omega_0 t} + 2\partial_t[f(t)]\partial_t[A(t)e^{j\omega_0 t}] + f(t)\partial_t^2[A(t)e^{j\omega_0 t}].\end{aligned} \tag{2.7}$$

We consider modulating signals with frequency components up to 1 THz (=1/ps). For the comparison we can thus take $f(t) = \sin(\omega_{\mathrm{RF}} t)$, with $\omega_{\mathrm{RF}} = 2\pi f_{\mathrm{RF}} \leq 2\pi/\mathrm{ps}$, and have

$$\begin{aligned}|\partial_t f| &\sim \omega_{\mathrm{RF}},\\ |\partial_t^2 f| &\sim \omega_{\mathrm{RF}}^2.\end{aligned}$$

Further, a light source with wavelength $\lambda_0 = 1.55\,\mu\mathrm{m}$ is used, so that the carrier frequency is $\omega_0 = 2\pi c/\lambda_0 \approx 2\pi \cdot 190/\mathrm{ps}$. The fastest variations in A will be due to the modulating signal at the center of the pulse, and due to chirp (explained in Section 2.2.2) in the tails of the pulse. As these are clearly slower than the carrier frequency, we get

$$\begin{aligned}|\partial_t[Ae^{j\omega_0 t}]| &\sim \omega_0,\\ |\partial_t^2[Ae^{j\omega_0 t}]| &\sim \omega_0^2.\end{aligned}$$

The orders of magnitude of the three terms in the right hand side of (2.7) are then, respectively, ω_{RF}^2, $\omega_{\mathrm{RF}}\omega_0$, and ω_0^2, and the relative error caused by the approximation (2.6) is approximately $2\omega_{\mathrm{RF}}/\omega_0$. This is a negligible error for low modulating frequencies, but reaches the appreciable level of $2/190 \approx 1\%$ at the highest frequencies (1 THz) considered in the OptoScope project. For the EOM simulations we should thus not use the approximation (2.6).

2.1.3 Boundary conditions and initial values

Boundary conditions The following continuity conditions must be satisfied at the interface between two media, indexed 1 and 2 [9]:

$$\begin{aligned} \mathbf{n} \times (\mathbf{E}_1 - \mathbf{E}_2) &= \mathbf{0}, & \mathbf{n} \times (\mathbf{H}_1 - \mathbf{H}_2) &= \mathbf{J}_{\mathrm{s}}, \\ \mathbf{n} \cdot (\mathbf{D}_1 - \mathbf{D}_2) &= \rho_{\mathrm{s}}, & \mathbf{n} \cdot (\mathbf{B}_1 - \mathbf{B}_2) &= 0, \end{aligned} \tag{2.8}$$

where $\mathbf{n}$ is the unit normal vector of the interface pointing into medium 2, and ρ_{s} and $\mathbf{J}_{\mathrm{s}}$ are surface charge density and surface current density, respectively, at the interface. These conditions are of interest in the EOM context at the interface between core and cladding materials of the optical waveguide, where ρ_{s} and $\mathbf{J}_{\mathrm{s}}$ are zero. For the electric field, the conditions imply that the component tangential to the interface is continuous, while the normal component has a discontinuity, proportional in size to the refractive index difference Δ.

In closed waveguides, the domain in which Maxwell's equations govern light propagation is bounded by a physical boundary: the metallic wall of the guide. An idealized metallic wall is represented by a perfect electric conductor[1] (PEC), which cannot sustain internal fields. The conditions (2.8) then reduce to the PEC boundary conditions

$$\begin{aligned} \mathbf{n} \times \mathbf{E} &= \mathbf{0}, & \mathbf{n} \times \mathbf{H} &= \mathbf{J}_{\mathrm{s}}, \\ \mathbf{n} \cdot \mathbf{D} &= \rho_{\mathrm{s}}, & \mathbf{n} \cdot \mathbf{B} &= 0. \end{aligned} \tag{2.9}$$

Open dielectric waveguides have no physical boundary. If no radiation or scattering of the optical field into the cladding is expected, the domain may be truncated in the transverse directions at a distance from the core, large enough for the field to decay to a negligible magnitude before reaching it. Then homogeneous Dirichlet or Neumann conditions can be used at the artificial boundary without influencing the field. However, if scattered waves reach such a boundary, they are reflected back into the domain. To avoid this, absorbing boundary conditions (ABCs) must be used, i.e., boundary conditions absorbing waves which reach the boundary. ABCs are also needed to truncate the domain in the longitudinal direction of the waveguide (chosen, by convention, to be aligned with the z axis). The most common type of ABCs used for optical waveguides are perfectly matched layers (PMLs), first introduced by Berenger [11] for the finite-difference time-domain method. They are discussed in the context of waveguide analysis by the finite

[1] Real metals are imperfect conductors, and may be modeled more correctly by impedance boundary conditions [10], a type of Robin boundary conditions. Such conditions are beyond the scope of this work.

element method in [12]. The idea is to introduce a layer near the truncating boundary with material parameters artificially modified to be absorbing. Waves thus decay as they travel through the layer, and PEC conditions may be used at the truncating boundary, placed outside the absorbing layer, without reflections reaching back into the domain in a non-physical way.

Initial conditions The problem is driven by an initial condition; the initial optical field fed into the waveguide. The characteristics of a typical input pulse for the EOM considered in the OptoScope project are given in the example at the end of Section 2.2.2. Physically, it is only meaningful to describe the initial value as given in all of the spatial domain at $t = t_0$. Mathematically, the roles of t and z may be interchanged, in which case the initial condition is given at $z = z_0$ over the (Cartesian product of the) temporal and transverse spatial domains, and boundary conditions are specified for the boundary of this product domain.

2.2 Propagation in straight optical waveguides

The governing wave equation, including time-dependent permittivity due to modulation, in combination with boundary conditions and initial conditions, specify the mathematical formulation of the optical EOM simulation problem, stated technically in Section 1.2. Before considering the full problem of optical pulse propagation in an EOM, however, we discuss in this section two related problems: the waveguide mode problem, concerning optical beam propagation in straight waveguides, and pulse propagation in optical fibers. Both problems are exemplified by special cases, in which analytic solutions exist.

2.2.1 Propagating modes

Mode analysis is in itself a large topic. Here we will only touch upon the very basics, to gain an idea about how light propagates through optical waveguides.

Optical waveguides support a discrete set of propagating modes. These are solutions to Maxwell's equations, with harmonic time-dependence and variation in the direction of propagation (to which the z axis is, by convention, aligned) given by a propagation constant $\gamma = \alpha + j\beta$. The electric field can then be written

$$\mathbf{E}(x, y, z; t) = \mathrm{re}\left(\mathbf{E}^0(x, y)e^{j\omega t - \gamma z}\right),$$

where ω is the angular frequency, and $\mathbf{E}^0$ is the mode shape, depending only on the transverse coordinates, x and y. This is equivalent to saying that the phasor solving Helmholtz's equation, derived in Section 2.1.1, can be written

$$\mathbf{E}(x, y, z) = \mathbf{E}^0(x, y)e^{-\gamma z}.$$

The mode problem is derived by using this assumption in Helmholtz's equation for the electric field, or an analogous one for the magnetic field. For given ω, the

resulting mode problem is an eigenproblem, solved for eigenvectors, i.e., transverse mode shapes $\mathbf{E}^0(x, y)$, and eigenvalues, from which the corresponding propagation constants γ of the modes are computed. The geometry of the waveguide is given by the transverse dependence of ε, and by appropriately chosen boundary conditions. In general, the mode problem cannot be solved analytically, but approximate methods must be used. In some special cases, however, analytic expressions can be found. Next we discuss two such cases, first a metallic, rectangular waveguide, and then a dielectric slab waveguide. We use these examples on the one hand to gain a feeling for the concept of modes, and on the other hand to introduce some terminology frequently encountered in waveguide analysis, such as effective index and cutoff frequency. For easier notation we drop the superscript, and write $\mathbf{E}$ for $\mathbf{E}^0$. In most cases we assume lossless materials, which results in $\alpha = 0$. When there is no risk of ambiguity, we then use the term propagation constant to refer to β, rather than to $\gamma = j\beta$.

Metallic rectangular waveguide Consider a rectangular waveguide, consisting of a lossless, homogeneous dielectric core, enclosed by a perfectly (electrically) conducting wall. We denote the waveguide width (along x) by a, and the height (along y) by b. It can be shown that in such a waveguide, two types of modes exist: transverse magnetic (TM) modes having $H_z = 0$, and transverse electric (TE) modes with $E_z = 0$ [6]. The mode problem reduces to a scalar problem,

$$\Delta_\perp \phi + h^2 \phi = 0, \tag{2.10}$$

where $\Delta_\perp = \partial_x^2 + \partial_y^2$, $h^2 = k^2 + \gamma^2$, and $k = k_0\sqrt{\varepsilon\mu}$ is constant since the core is homogeneous. The equation is solved for $\phi = E_z$ in the TM case and for $\phi = H_z$ in the TE case.

The PEC boundary conditions (2.9) reduce to homogeneous Dirichlet conditions for E_z and homogeneous Neumann conditions for H_z, leading to different eigenvectors in the two cases. The eigenvalues are equal in both cases, and turn out to be

$$h_{mn}^2 = \left(\frac{m\pi}{a}\right)^2 + \left(\frac{n\pi}{b}\right)^2, \tag{2.11}$$

where for TM modes, $m = 1, 2, 3, \ldots$, and $n = 1, 2, 3, \ldots$, while for TE modes either m or n, but not both, may also be 0. The mode shapes, or eigenvectors, are

$$E_z(x, y) = E_0 \sin\left(\frac{m\pi}{a}x\right) \sin\left(\frac{n\pi}{b}y\right),$$
$$H_z(x, y) = H_0 \cos\left(\frac{m\pi}{a}x\right) \cos\left(\frac{n\pi}{b}y\right)$$

for TM and TE modes, respectively. The remaining components can be computed from E_z and H_z. The lowest order TM and TE modes are shown in Figures 2.1 and 2.2, respectively.

Since the medium is lossless, we have $\gamma = j\beta$, where β is real. On the other hand, the propagation constant of the (m, n) mode is given by

$$\gamma = j\beta = j\sqrt{k^2 - h_{mn}^2}.$$

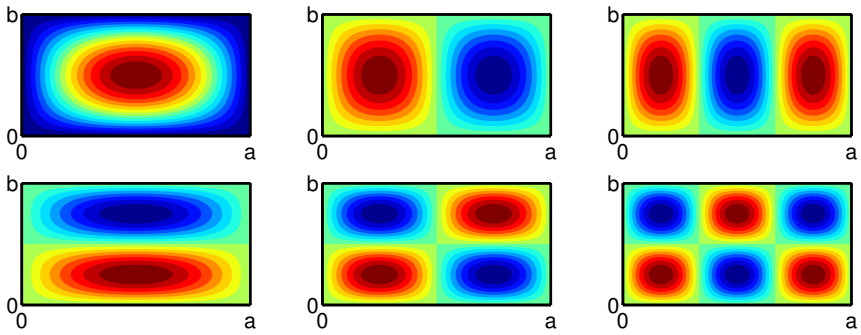

Figure 2.1: Contours of E_z component of transverse magnetic (TM_{mn}) modes over waveguide cross section. The rows (top to bottom) correspond to $m = 1, 2$, and the columns (left to right) correspond to $n = 1, 2, 3$.

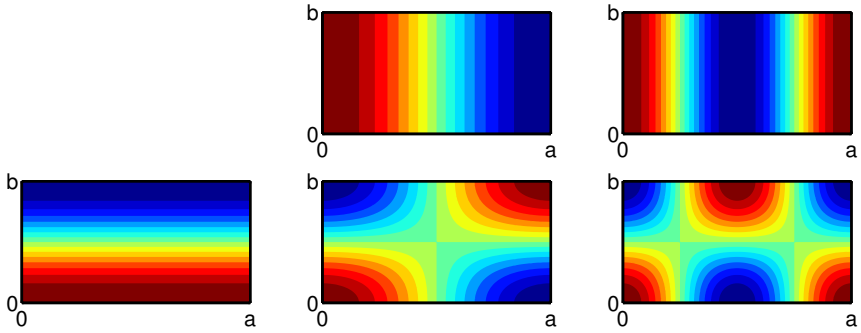

Figure 2.2: Contours of H_z component of transverse electric (TE_{mn}) modes over waveguide cross section. The rows (top to bottom) correspond to $m = 0, 1$, and the columns (left to right) correspond to $n = 0, 1, 2$.

Hence, the mode only exists for $k \geq (k_c)_{mn} := h_{mn}$, where h_{mn} is given by (2.11), and k_c is called the *cutoff wavenumber* of the mode. The cutoff condition may be expressed equivalently in terms of the *cutoff frequency* $\omega_c = ck_c$, or the *cutoff wavelength* $\lambda_c = 2\pi/k_c$. For a rectangular metallic waveguide with $a > b$, the mode with the lowest cutoff frequency is the TE_{10} mode, which is therefore called the dominant mode of the waveguide. At frequencies between the cutoff frequency of the dominant mode and that of the mode with the next lowest cutoff frequency a waveguide is said to operate as a single-mode waveguide, since it only supports the dominant mode.

Dielectric slab waveguide Our second example is a dielectric slab waveguide, consisting of a dielectric core layer with refractive index n_1, sandwiched between two dielectric cladding layers with refractive index $n_0 < n_1$. For simplicity we assume $\mu = 1$. The slab extends infinitely (theoretically) in the y direction, so that light is confined only in the x direction. Such a guide is not very useful from a practical viewpoint, but interesting for theoretical purposes, since it allows for

quasi-analytical computation of mode shapes in a dielectric waveguide, which is not possible for dielectric rectangular or rib waveguides.

In the mode problem, any derivative with respect to y vanishes, and it turns out that as in the rectangular metallic waveguide, two sets of modes, TM and TE, exist. Here, however, not only H_z vanishes in the TM case, but also E_y and H_x. Similarly, the TE modes have $E_z = H_y = E_x = 0$. The mode problem again reduces to the scalar equation (2.10), which is now one-dimensional, with $\phi = \phi(x)$ and $\Delta_\perp$ reduced to ∂_x^2. In the TM case, the problem is solved for $\phi = H_y$, from which the non-vanishing components E_x and E_z can be computed, and the TE mode problem is solved for $\phi = E_y$, from which H_x and H_z are computed.

We restrict the following discussion to TE modes. For a slab with core width $2a$, centered at $x = 0$, the TE mode shapes are given by [4]

$$E_y(x) = \begin{cases} E_1 e^{\alpha_x x} & x < -a \\ E_0 \cos(h_x x - \phi) & |x| \leq a \\ E_2 e^{-\alpha_x x} & x > a. \end{cases}$$

We see that the modes are confined inside the core, and decay exponentially in the cladding. The phase offset is $\phi = \frac{m\pi}{2}$. The amplitude E_0 corresponds to the optical intensity, while E_1 and E_2 are chosen such that E_y is continuous at the interfaces between core and cladding. The discrete set of modes is numbered by $m = 0, 1, 2, \ldots$, and mode parameters $h_{x,m}$ and $\alpha_{x,m}$ are found, for each m, by solving

$$\begin{cases} w = u \tan(u - \frac{m\pi}{2}) \\ u^2 + w^2 = v^2, \end{cases}$$

called the *dispersion equations*, for $u = ah_x$ and $w = a\alpha_x$, given the normalized frequency $v = k_0 a\sqrt{n_1^2 - n_0^2}$. These are nonlinear equations, and a numerical method must be used to solve the system, hence we say that the mode solutions are computed quasi-analytically. As for the rectangular metallic waveguide, we can then compute the propagation constant

$$\beta_m = \sqrt{k^2 - h_{x,m}^2},$$

where $k = k_0 n_1$.

The dimensionless quantity $n_{\text{eff}} = \beta/k_0$ is called the *effective index* of the mode, and satisfies $n_0 \leq n_{\text{eff}} < n_1$ for propagating modes, where the first inequality is the cutoff condition for a slab waveguide mode. In Figure 2.3 the first three modes are shown for frequencies just above their respective cutoff frequencies. Note how – unlike modes in a metallic waveguide – the mode shapes depend on frequency, so that at higher frequencies, the modes are more well-confined inside the core. The confinement also increases with increasing refractive index difference between core and cladding.

2.2.2 Pulse propagation and dispersion

We now make a short digression into the analysis of pulse propagation in optical fibers. This has two purposes: First, the lessons learned from such analysis serve as

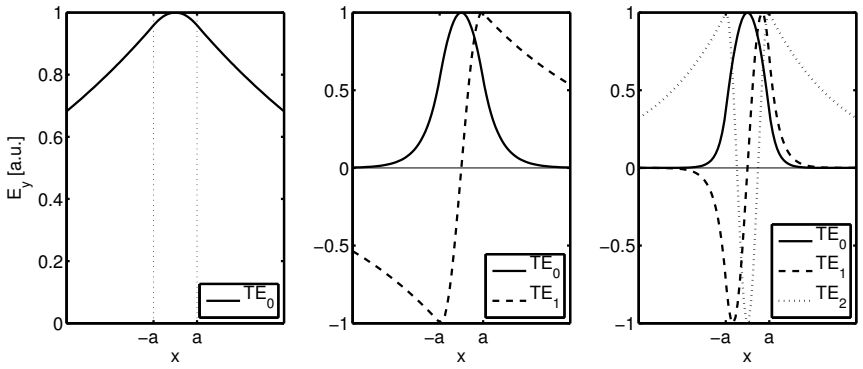

Figure 2.3: The first three TE modes of a slab waveguide. Frequencies are just above cutoff of TE_0 (left), just above cutoff of TE_1 (center) and just above cutoff of TE_2 (right). Interfaces between core and cladding are indicated by dotted lines in the left plot.

inspiration to the formulation of the moving-time time-domain beam-propagation method (TD-BPM), which is the numerical method mainly considered in this work. Second, it provides some background on the generation of chirped pulses, discussed at the end of the section, which is the type of pulses used as optical input to the EOMs considered in the OptoScope project.

The basic assumption made in the analysis of pulse propagation in fibers is that the transverse variables (x and y) can be separated from the longitudinal variable (z) and time, i.e., that the electric field can be represented by

$$\mathbf{E}(x,y,z;t) = \mathrm{re}\left(\mathbf{E}^0(x,y)A(z,t)e^{j(\omega_0 t-\beta_0 z)}\right), \tag{2.12}$$

where ω_0 is the carrier, or central, frequency of the pulse, β_0 is the propagation constant at ω_0, and $A(z,t)$, known as the "slowly varying pulse envelope", describes the shape of the pulse, as it propagates along the fiber. Inserting this Ansatz into the wave equation leads to two coupled equations, the mode equation for $\mathbf{E}^0$ and a pulse propagation equation for A.

The mode equation is solved in frequency domain for $\mathbf{E}^0(x,y)$ and $\beta(\omega)$, as described in Section 2.2.1. Strictly speaking, the mode shape $\mathbf{E}^0$ is also a function of ω, however, in the Ansatz this dependence is implicitly assumed to be negligible. This assumption, which is standard in optical fiber analysis, is shown in [13] to be valid for pulses as short as a few optical carrier cycles. The dependence of the propagation constant β on ω, on the contrary, cannot be neglected, but may rather have a strong impact on the propagation of pulses in fibers. This dependence is known as *dispersion*[2]. Since the exact form of the dependence is, in general, not known, a Taylor expansion about the carrier frequency ω_0,

$$\beta(\omega) = \beta_0 + \beta_1(\omega-\omega_0) + \tfrac{1}{2}\beta_2(\omega-\omega_0)^2 + \ \ldots,$$

[2]Dispersion has two sources: waveguide dispersion, due to geometry, and material dispersion, due to frequency dependence of the material's refractive index. Dispersion can therefore exist even when non-dispersive materials are considered.

where $\beta_m = \beta^{(m)}(\omega_0),\ m = 0, 1, \ldots$, is used. Terms of third and higher order can often be neglected if the optical field is quasi-monochromatic, i.e., if the spectral width is much smaller than the carrier frequency.

Under the same assumption of a quasi-monochromatic optical field, the pulse envelope A is slowly varying with respect to z, and $\partial_z^2 A$ can be neglected in the pulse propagation equation. The following equation is derived (see [7] for details)

$$\partial_z A = -\beta_1 \partial_t A - \frac{j\beta_2}{2}\partial_t^2 A + j\Delta\beta A.$$

The first term in the right hand side accounts for the propagation of the pulse envelope along z with the group velocity $v_\mathrm{g} = \frac{1}{\beta_1}$, and the third term includes nonlinear effects and fiber losses. The second term accounts for so called group velocity dispersion, which has three effects on the pulse: it broadens the pulse in time, it reduces the peak amplitude, and it adds *chirp* to the pulse, i.e., dependence of frequency on time.

It is customary to make the change of variables $\tau = t - z/v_\mathrm{g}$, which is discussed thoroughly in Section 3.2, in the context of the moving-time TD-BPM. The pulse propagation equation for optical fibers is then expressed as

$$\partial_z A = -\frac{j\beta_2}{2}\partial_\tau^2 A + j\Delta\beta A.$$

in a time frame moving with the group velocity. If fiber losses can be neglected, this equation is referred to as the nonlinear Schrödinger equation. When nonlinear effects are also negligible, the equation reduces to the linear Schrödinger equation

$$\partial_z A = -\frac{j\beta_2}{2}\partial_\tau^2 A. \tag{2.13}$$

Propagation of Gaussian pulses in lossless linear dispersive fibers The linear Schrödinger equation (2.13), governing propagation of pulses in lossless linear dispersive fibers, can be solved analytically for Gaussian initial pulses,

$$A(0, \tau) = \exp\left(-\frac{\tau^2}{2\tau_0^2}\right).$$

Here τ_0 is the half-width at $1/e$-intensity point[3]. The solution is then [7]

$$\begin{aligned} A(z, \tau) &= \frac{\tau_0}{(\tau_0^2 - j\beta_2 z)^{1/2}} \exp\left(-\frac{\tau^2}{2(\tau_0^2 - j\beta_2 z)}\right) \\ &= a(z) \exp\left(-\frac{(1 + jC(z))}{2}\frac{\tau^2}{\tau_1^2(z)}\right), \end{aligned} \tag{2.14}$$

[3]Another common measure of pulse width is the full width at half maximum $\tau_\mathrm{FWHM} = 2\sqrt{\ln 2}\tau_0$.

where from the latter formulation it is clear that the shape of the propagated pulse is still Gaussian, with a z-dependent half-width $\tau_1(z)$ and complex amplitude $a(z)$. Introducing the dispersion length $L_\mathrm{D} = \tau_0^2/|\beta_2|$, we can write

$$\tau_1(z) = \tau_0\sqrt{1 + (z/L_\mathrm{D})^2}.$$

We see that L_D is the distance at which the pulse has broadened by a factor $\sqrt{2}$.

At fixed z, the instantaneous frequency of $\mathbf{E}$ is the time derivative of the phase, given by (2.12) and (2.14) as

$$\omega(\tau) = \partial_\tau\left(\omega_0\tau - \frac{C\tau^2}{2\tau_1^2} + \text{constant}\right) = \omega_0 - \frac{C\tau}{\tau_1^2}. \tag{2.15}$$

The frequency thus depends linearly on τ, or, expressed in different terms, the pulse is *linearly chirped*. The chirp rate, i.e., the rate of change of frequency with time, is proportional to $C(z) = \mathrm{sgn}(\beta_2)\frac{z}{L_\mathrm{D}}$.

Example: Generation of EOM input pulse An optical input pulse to the EOM considered in the OptoScope project is generated by propagating an initially unchirped Gaussian pulse with $\tau_0 = 80\,\mathrm{fs}$ and carrier wavelength $\lambda_0 = 1.55\,\mu\mathrm{m}$ (corresponding to $\omega_0 = 2\pi c/\lambda_0 \approx 1200\,(\mathrm{ps})^{-1}$), through 1 km of dispersive fiber with group velocity dispersion parameter $\beta_2 \approx 50\,(\mathrm{ps})^2/\mathrm{km}$. Then we have, approximately, $L_\mathrm{D} = 0.13\,\mathrm{m}$, and at the end of the fiber, i.e., at $z = 1\,\mathrm{km}$,

$$C = z/L_\mathrm{D} = 7800,$$
$$\tau_1 = 7800\tau_0 = 620\,\mathrm{ps}$$

(note the very high stretch factor), which are thus the characteristics of the input pulse to the EOM. The normalized envelope of the pulse, before and after dispersion, is illustrated in Figure 2.4. The real part of the chirped pulse is shown, although, due to the high chirp rate, the oscillations are not visible. The white line segments inside the pulse are merely graphical artefacts. The inset shows the oscillations at the center of the pulse. Note that the oscillations are due to chirp only; the carrier frequency ω_0 has been factored out in (2.12).

The dispersive fiber in this example corresponds to the "Group Velocity Dispersion D_1" box in Figure 1.1. The pulses before and after that box represent the pulses in Figure 2.4, and we can now appreciate that the horizontal, rather than vertical, spread of the color spectrum after dispersion illustrates chirp.

To see to what extent the chirp affects the instantaneous frequency in this example, we rewrite (2.15) as

$$\omega(\tau) = \omega_0 - \frac{C}{\tau_1}\frac{\tau}{\tau_1} = \omega_0 - \frac{1}{\tau_0}\frac{\tau}{\tau_1} \approx \left(1200 - 12\frac{\tau}{\tau_1}\right)(\mathrm{ps})^{-1}.$$

Hence, at $\tau = \pm\tau_1$, the instantaneous frequency is changed away from ω_0 by about $\mp 1\%$.

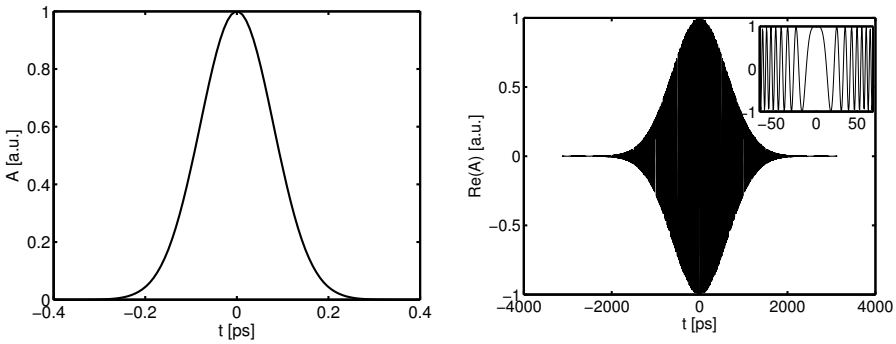

(a) Before dispersion

(b) After dispersion (input to the EOM)

Figure 2.4: Pulse envelopes with normalized amplitude. The real part of the chirped pulse is shown, and the inset shows the center part of the pulse.

Chapter 3

Methods

EOM modeling has two main parts: propagation of the electric (modulating) signal along the electrodes, and propagation of the optical (modulated) pulse along the dielectric waveguide. As previously stated, this work is limited to the optical propagation problem, where we assume that the refractive index is a known function of space and time, due to modulation. In the previous chapter we discussed analytic solutions to some problems encountered in the analysis of optical waveguides. In most practical applications, however, no analytic solutions are available, and numerical methods must be used. Such methods are the subject of this chapter.

A basic optical model of TW-EOMs is given by considering propagation of the pulses only in the two arms. The amplitude-modulated output of the EOM is then computed by simply adding the output of the two arms, with and without phase-modulation, or with phase-modulation of opposite signs, in the case of push-pull modulators. In this approach the optical problem is restricted to propagation in straight waveguides, and separation of variables may be used. Similar to optical fiber analysis, described in Section 2.2.2, the problem splits into a mode problem for the propagation constant and the x- and y-dependent mode shape, and a propagation problem for the z- and t-dependent pulse envelope. The mode problem must, in general, be solved numerically, using, e.g., the finite element method [9]. The propagation problem under modulation is seen as a perturbation to mode propagation. Then a local phase shift, proportional to the refractive index shift, δ_n, can be computed and accumulated along z, to find the total phase shift at the end of the arm, [14–16].

This model describes an (optically) ideal modulator, which would, in the absence of a modulating signal, leave the input pulse unchanged. However, in any real device, the output pulse is damped due to optical losses (not to be confused with damping of the electric signal along the electrodes, which is also a concern in TW-EOM design), such as losses in couplers and waveguide bends. An enhanced model is therefore sometimes used, in which damping is accounted for by multiplying the output pulse by a constant damping factor. The damping is computed

in frequency domain, at the carrier frequency, using different methods for different types of losses. Bend losses have, e.g., been treated using the beam-propagation method (BPM) [17], and conductor losses, i.e., losses due to the optical field reaching into the electrode, which is an imperfect conductor, have been computed using a mode solver and perturbation method [18]. In [19], losses specific for EOM structures are considered, e.g., losses due to mode mismatch between the input/output region of the EOM, and the active region, where the presence of electrodes along the waveguide modify the mode shape.

Based on simplifying assumptions, an approach of the described type thus subdivides the optical propagation problem, extending over space and time, into several sub-problems, extending over fewer dimensions; the mode problem is solved over x and y, the modulated propagation problem over z and t, and the damping problems over x, y and sometimes z. The major benefit of such an approach is clearly its computational efficiency, compared to resolving the full problem in space and time. Further, it allows for design optimization of individual parts of the EOM in a modular manner. On the other hand, it requires knowledge about different methods for the different sub-problems. A more severe drawback is the simplifications employed. Justifying them requires a priori knowledge about the relative importance of various effects, which may pose a problem when considering new designs.

In this work, the following alternative is considered: a method resolving the full problem in space and time. Such methods discretize and solve the wave equations in a more direct way, but are computationally intense. However, with the ever-growing computational power and memory storage of computers, the problem sizes, generated by the very large size of the device compared to the optical wavelength, are about to go from unthinkable to realistic. Still, general purpose methods, such as the finite-difference time-domain (FDTD) method, are too expensive, and methods more adapted to the problem at hand are needed, such as the time-domain beam-propagation method (TD-BPM). Several versions of the TD-BPM exist. In Section 3.1.2 one version, which we refer to as the slow-wave TD-BPM, is briefly described, along with the FDTD method. Our main interest, however, is in the version we call the *moving-time TD-BPM*, to which most of this chapter is devoted. Its derivation is based on the works by Masoudi *et al.* [20, 21], but a different paraxial approximation is suggested, which is shown to increase the accuracy of the method without adding to the computational cost. Further, while Masoudi *et al.* use finite differences for the discretization, we present here a discretization based on tensor-product finite elements.

Before considering space- and time-resolving methods, we introduce the BPM in Section 3.1.1, since it is a standard tool in optical waveguide analysis, and, in addition, forms the basis of the TD-BPMs.

3.1 Preliminaries

3.1.1 BPM

The beam propagation method (BPM) is a well established frequency-domain method used in optical and acoustical wave propagation when there is an assumed propagation direction, taken to be along the positive z axis, and a specified frequency. In the scalar case, the following Ansatz is used:

$$E(x, y, z; t) = \mathrm{re}\left(\psi(x, y, z)e^{j(\omega t - k_0 n_\mathrm{p} z)}\right), \tag{3.1}$$

where $k_0 = \omega/c$, and n_p is a method parameter to be chosen appropriately. The phase index is a natural choice, if known. Otherwise the refractive index of the cladding may be used. Inserting this Ansatz into the scalar wave equation (2.5) and dividing by the common phase factor yields the BPM equation

$$\partial_z^2\psi - 2jk_0 n_\mathrm{p}\partial_z\psi = -k_0^2(n^2 - n_\mathrm{p}^2)\psi - \Delta_\perp\psi, \tag{3.2}$$

where $\Delta_\perp = \partial_x^2 + \partial_y^2$ is the transverse Laplacian. The equation is discretized in the transverse direction using, e.g., finite differences, and an initial field given at $z = z_0$ is propagated along z using an explicit or implicit scheme.

The geometry of the problem is prescribed by the spatial dependence of the refractive index n. In free space $n = 1$, and if n_p is chosen to be 1 as well, the first term of the right hand side vanishes. We thus see that the second term governs propagation in free space. In a lossless waveguide, homogeneous along z, the envelope of a propagating mode is theoretically constant along z. If the mode shape is taken as initial field and the effective index of the mode is chosen for n_p, then any variation of ψ along z is due to numerical (discretization or rounding) errors. If the geometry varies slowly along z, ψ can be assumed to do so too, and the $\partial_z^2\psi$ term can be neglected, which is known as the *paraxial approximation*.

Many versions of the BPM exist, including paraxial and non-paraxial versions, scalar and vectorial versions, and versions based on finite differences and finite elements for discretization in the transverse direction. For an account of several of these BPMs, see [22, Chapter 2] and references therein.

3.1.2 Space- and time-resolving methods

For electromagnetic simulations in time domain with resolution in all spatial dimensions, the finite-difference time-domain method (FDTD) [23] is a standard tool. The wave equation is discretized with finite differences, and the field is propagated in time by an explicit time-stepping scheme. The method is simple to implement, flexible and very efficient for problems with spatial dimensions on the scale of the wavelength [24]. However, because of the explicit time-stepping, a small time step must be chosen to satisfy the Courant-Friedrichs-Lewy (CFL) stability condition. Hence, for three-dimensional optical devices with long interaction distances compared to the wavelength, such as EOMs, the FDTD method becomes very expensive in terms of computer resources.

As an alternative to the FDTD method, several different time-domain beam-propagation methods (TD-BPMs) have been developed for the propagation of pulses in optical devices. The most wide-spread of these, referred to here as the slow-wave TD-BPM, was developed originally in [25–27]. It uses the Ansatz

$$E(x, y, z; t) = \mathrm{re}\left(\psi(x, y, z; t)e^{j\omega_0 t}\right) \tag{3.3}$$

in the wave equation, and employs the *slowly varying envelope approximation* (SVEA),

$$|\partial_t^2 \psi| \ll \omega_0 |\partial_t \psi|, \tag{3.4}$$

in the resulting TD-BPM equation, so that the second order time derivative may be dropped. The SVEA is valid for temporally broad pulses, or, equivalently, pulses with narrow spectral bandwidth. The early slow-wave TD-BPMs are discretized by finite differences, while in an alternative version finite elements are used for the spatial discretization [28, 29]. To avoid the restriction of the SVEA, broadband TD-BPMs have been developed, which include the second order time derivative by using Padé approximants [28, 30].

The described TD-BPMs have been successfully applied to many optical structures and devices, typically with dimensions comparable to the optical wavelength. However, like the FDTD method, these methods are less suited for propagation over long distances, since all spatial dimensions must be resolved in each time step, leading to high computational costs for long devices.

3.2 Moving-time TD-BPM

As described in Section 2.2.2, a time window moving with the pulse as it propagates is a standard, necessary tool in optical fiber analysis. In that context, propagation distances are on the order of kilometers. To handle structures which are much shorter than long-haul optical fibers, yet very long compared to the optical wavelength, such as EOMs, Masoudi *et al.* introduce a similar moving time window in the context of TD-BPM [20]. We refer to their method as the moving-time TD-BPM. In Section 3.2.1, a detailed derivation of the scalar version is given, and some features of the method are discussed. In addition, we suggest a different paraxial approximation than the one used by Masoudi *et al.* Our formulation is derived by introducing the moving time window *before* neglecting second order derivatives involving the propagation direction, while Masoudi *et al.* do the same procedures in the opposite order. The new formulation requires no additional computational effort, yet it is shown in Chapter 4 to drastically increase the accuracy of the method, especially for short pulses. In Section 3.2.2, a more general formulation is derived, including both the scalar and the vector versions. The weak form of this general equation is given in Section 3.2.3. Based on the weak form, the equation is discretized in the transverse directions and time using tensor product finite elements. The solution is stepped forward along z using an implicit scheme, the midpoint method. These discretizations are described in Section 3.2.4.

3.2.1 Derivation of the scalar equation

In a series of papers Masoudi *et al.* have developed a version of TD-BPM with a moving time window following the pulse with the group velocity [20, 21, 31–33]. Their derivation is based on an Ansatz similar to the BPM Ansatz (3.1),

$$E(x,y,z;t) = \mathrm{re}\left(\psi(x,y,z;t)e^{j(\omega_0 t - k_0 n_\mathrm{p} z)}\right), \tag{3.5}$$

with the difference that here ψ varies not only with space but also with time, to allow for pulse shapes and, more importantly in our case, time-dependent modulation. This Ansatz differs from the one used for the slow-wave TD-BPM, (3.3), in that it factors out not only the time oscillations $e^{j\omega_0 t}$, but also oscillations along the assumed propagation direction z. Then, for temporally broad pulses, not only the SVEA (3.4) holds, but also the approximation

$$|\partial_z^2 \psi| \ll k_0 n_\mathrm{p} |\partial_z \psi|, \tag{3.6}$$

if the geometry varies slowly along z, and n_p is appropriately chosen. This corresponds to the paraxial approximation in the case of BPM.

Inserting (3.5) into the scalar wave equation (2.5), and dividing by the common phase factor, yields

$$\partial_z^2 \psi - 2jk_0 n_\mathrm{p} \partial_z \psi = \frac{n^2}{c^2}\partial_t^2 \psi + 2jk_0 \frac{n^2}{c}\partial_t \psi - k_0^2 (n^2 - n_\mathrm{p}^2)\psi - \Delta_\perp \psi, \tag{3.7}$$

where we have assumed for simplicity that $\mu = 1$, and that $\varepsilon = n^2$ is independent of time; the general case will be treated in the next section. We see that the TD-BPM equation (3.7) is the BPM equation (3.2), with two additional terms for the first and second time derivatives of ψ. Like the BPM equation, the (moving-time) TD-BPM equation is propagated in z, while treating time as an additional "transverse" variable.

Next the moving time window is introduced by replacing the ordinary time variable by a moving time variable, τ, moving with the group velocity, v_g, of the pulse. The same change of variables is standard in the analysis of optical fibers, as mentioned in Section 2.2.2. We state it here as

$$\begin{cases} \zeta = z \\ \tau = t - n_\mathrm{g} z/c, \end{cases} \tag{3.8}$$

where we prefer to use the group index $n_\mathrm{g} = c/v_\mathrm{g}$, rather than the group velocity, for better readability. By the chain rule we have

$$\begin{aligned} \partial_z &= \partial_\tau \frac{\partial \tau}{\partial z} + \partial_\zeta \frac{\partial \zeta}{\partial z} = \partial_\zeta - \frac{n_\mathrm{g}}{c}\partial_\tau, \\ \partial_t &= \partial_\tau \frac{\partial \tau}{\partial t} + \partial_\zeta \frac{\partial \zeta}{\partial t} = \partial_\tau, \end{aligned}$$

and for the second order derivatives

$$\partial_z^2 = \partial_\zeta^2 - \frac{2n_\mathrm{g}}{c}\partial_\tau\partial_\zeta + \frac{n_\mathrm{g}^2}{c^2}\partial_\tau^2,$$
$$\partial_t^2 = \partial_\tau^2.$$

In the new variables, the moving-time TD-BPM equation then reads

$$\partial_\zeta^2\psi - \frac{2n_\mathrm{g}}{c}\partial_\tau\partial_\zeta\psi - 2jk_0n_\mathrm{p}\partial_\zeta\psi = \frac{n^2 - n_\mathrm{g}^2}{c^2}\partial_\tau^2\psi + 2jk_0\frac{n^2 - n_\mathrm{g}n_\mathrm{p}}{c}\partial_\tau\psi - k_0^2(n^2 - n_\mathrm{p}^2)\psi - \Delta_\perp\psi, \quad (3.9)$$

where the difference compared to (3.7) lies in the three added terms involving the factor n_g.

An advantage of the moving-time TD-BPM, compared to the slow-wave TD-BPM, is related to the size of the computational domain to be discretized. With the latter method, the full length of the device must be resolved for each discrete time step from 0 to the total travel time, T. On the contrary, with the former method, only the moving time window $I_\tau = [-M\tau_0, M\tau_0]$ needs to be resolved at each discrete ζ step along the device. Here τ_0 is the temporal half-width of the pulse (see Section 2.2.2), and M is a moderate number of pulse widths chosen large enough to let the pulse vanish (numerically) before reaching the time-window edges. This makes the moving-time TD-BPM particularly efficient for propagation of short pulses over long distances, i.e., when $T \gg \tau_0$.

The change of coordinates is illustrated graphically in Figure 3.1. Arbitrary length and time units are used, and the group velocity is normalized, $v_\mathrm{g} = 1\,\mathrm{l.u./t.u.}$ In the left part of the figure, the old and new coordinate axes, (z, t) and (ζ, τ), are shown, along with contour lines of the magnitude of a Gaussian pulse, propagating in a straight waveguide. The pulse propagation is given by (2.14), with $\tau_0 = 0.1\,\mathrm{t.u.}$ and $\beta_2 = 0.005\,\mathrm{t.u.}^2/\mathrm{l.u.}$, implying $L_\mathrm{D} = 2\,\mathrm{l.u.}$ The geometrical interpretation of partial derivative with respect to ζ, ∂_ζ, is the rate of change when ζ increases, while τ is kept constant, i.e., the directional derivative along the vector $\mathbf{v}$, perpendicular to the τ axis, indicated in the right part of the figure. Analogously, ∂_τ is the directional derivative along $\mathbf{u}$.

Paraxial approximation In the BPM, the paraxial approximation (3.6) holds whenever the waveguide varies slowly with z. However, as is clear from Figure 3.1, when the pulse envelope varies rapidly with time, it also varies rapidly with z due to propagation, and (3.6) does not hold, even for straight waveguides. The change from ordinary to moving time frame separates these dependencies in an eligible way; the pulse shape is taken into account by τ derivatives, while only *changes* to the shape, as the pulse propagates along the line $z = v_\mathrm{g}t$, are captured by ζ derivatives. Still, for short pulses $\partial_\zeta\psi$ is indirectly influenced by the pulse shape through the dependence of L_D on τ_0. In time domain it would, in the author's

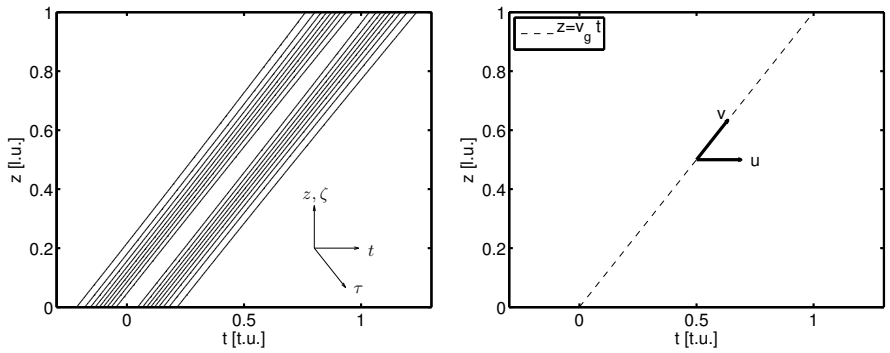

Figure 3.1: Illustration of change of coordinates with arbitrary length units (l.u.) and time units (t.u.). Left: Coordinate axes for (z, t) and (ζ, τ) with $v_\mathrm{g} = 1\,\mathrm{l.u./t.u.}$, and contour lines of the amplitude of a Gaussian pulse propagating according to (2.14) ($\tau_0 = 0.1\,\mathrm{t.u.}$, $L_\mathrm{D} = 2\,\mathrm{l.u.}$). Right: $\mathbf{u}$ and $\mathbf{v}$ are parallel to $z = 0$ and $z = v_\mathrm{g}t$, and represent, respectively, the directions along which ∂_τ and ∂_ζ measure rate of change.

opinion, be more appropriate to refer to

$$|\partial_\zeta^2 \psi| \ll k_0 n_\mathrm{p} |\partial_\zeta \psi|$$

as the paraxial approximation, as it holds for waveguides varying slowly with z, with less sensitivity to the pulse shape than (3.6). The corresponding paraxial moving-time TD-BPM equation is obtained from (3.9) by neglecting only the term $\partial_\zeta^2 \psi$.

In [20, 21], Masoudi *et al.* present what they call the paraxial version of the moving-time TD-BPM, in which they neglect the entire term

$$\partial_z^2 \psi = \partial_\zeta^2 \psi - \frac{2n_\mathrm{g}}{c} \partial_\tau \partial_\zeta \psi + \frac{n_\mathrm{g}^2}{c^2} \partial_\tau^2 \psi. \tag{3.10}$$

Considering the comments just made, it is thus not surprising that their method shows good accuracy for pulses with width $\geq 100\,\mathrm{ps}$, but fails to do so for shorter pulses. It should be noted, that neglecting the term $\frac{n_\mathrm{g}^2}{c^2} \partial_\tau^2 \psi$ cannot be motivated by the pulse traveling approximately along the z axis. What is more, there is no computational gain in neglecting it, since it represents merely a modification of the coefficient of the $\partial_\tau^2 \psi$ term; the term is still present in the simplified equation.

For waveguides varying slowly with z then, the first term in the right hand side of (3.10) may be neglected, whereas the third term should be kept. It is less clear how to handle the second term. It does add to the complexity of the equation, and complicates the stability analysis. It can be argued that the term is in general smaller in magnitude than the term $2jk_0 n_\mathrm{p} \partial_\zeta \psi$, but whether or not it is negligible depends on the data, such as pulse shape, in the specific case. In the current work we implement a simplified paraxial moving-time TD-BPM equation, which neglects the first and second term of (3.10). The equation then reads

$$2jk_0 n_\mathrm{p} \partial_\zeta \psi = -\frac{n^2 - n_\mathrm{g}^2}{c^2} \partial_\tau^2 \psi - 2jk_0 \frac{n^2 - n_\mathrm{g} n_\mathrm{p}}{c} \partial_\tau \psi + k_0^2 (n^2 - n_\mathrm{p}^2) \psi + \Delta_\perp \psi. \tag{3.11}$$

In Section 4.1 a comparison is made between this version and the paraxial version of Masoudi *et al.* in the case of propagation in a straight slab waveguide. As expected, the results show clearly the superiority of the version presented here, while, as pointed out, there is no difference in computational cost between the two methods. Equation (3.11) has in fact been implemented previously, and results are reported, and compared to the results by Masoudi *et al.*, in [34]. There, however, no comment is made on the difference in formulation between the two equations, but rather the improved results are attributed to the use of finite elements instead of finite differences for discretization. In view of the discussion above, this seems to be an erroneous conclusion.

In two later papers [31,32], Masoudi develops a non-paraxial version of the TD-BPM, based on Padé approximants for the inclusion of the $\partial_\zeta^2\psi$ term. However, the terms including $\partial_\tau\partial_\zeta\psi$ and $\partial_\tau^2\psi$ are still neglected. The non-paraxial method shows surprisingly improved results, compared to the paraxial version, in view of the still lacking terms.

In the context of EOM simulation, the width of the optical pulse is of the same order of magnitude as the total time it takes the peak to travel through the device. Hence, the moving time window to be resolved is not smaller than the time interval used in the fixed time frame. Rather, the gain of using a moving time frame is related to the time-dependent modulation, which varies very rapidly with time, compared to the pulse width. As for short pulses, described above, these rapid pulse shape variations contribute to ∂_t^2, ∂_z^2, and ∂_τ^2, but not to ∂_ζ^2, such that the paraxial approximation may be used in the moving time frame, but not in the fixed time frame.

3.2.2 Abstract formulation

We now derive the TD-BPM in a more abstract way, including both the scalar and vector versions. In order to be able to use the Ansatz (3.5) we split the spatial derivative in the (electric) wave equation into its longitudinal and transverse components in the following way

$$\left.\begin{array}{c} -\nabla\cdot(\mu^{-1}\nabla\phi) \\ \nabla\times(\mu^{-1}\nabla\times\phi) \end{array}\right\} = (-\mathcal{Q}_1\partial_z^2 + \mathcal{Q}_2\partial_z + \mathcal{Q}_3)\phi \tag{3.12}$$

where $\mathcal{Q}_1$ is a scaling factor, and $\mathcal{Q}_2$ and $\mathcal{Q}_3$ are transverse differential operators, specified below for the scalar and vector case, respectively. The relative permeability μ is unity in our applications, however, it is included here since the formulation of perfectly matches layers (PMLs) is based on an artificial choice of space-dependent permittivity and permeability near the boundary of the computational domain. The dependence is in the transverse directions, so $\partial_z\mu = 0$, which is used in the derivation of the $\mathcal{Q}$ operators. In the scalar case, then,

$$\begin{aligned} \mathcal{Q}_1 &= \mu^{-1}, \\ \mathcal{Q}_2 &= 0, \\ \mathcal{Q}_3 &= -\nabla_\perp\cdot(\mu^{-1}\nabla_\perp), \end{aligned}$$

where $\nabla_\perp = (\partial_x, \partial_y, 0)$, which is derived in a straightforward manner by writing $\nabla = \nabla_\perp + \hat{z}\partial_z$, and expanding the product in (3.12). Similarly, the curl operator for the vector equation can be written in matrix form, and split into a sum of two terms, for the transverse and longitudinal partial derivatives, respectively. We use the notation

$$\nabla\times = \begin{bmatrix} 0 & -\partial_z & \partial_y \\ \partial_z & 0 & -\partial_x \\ -\partial_y & \partial_x & 0 \end{bmatrix} = R_\perp + J_z\partial_z,$$

where

$$R_\perp = \nabla_\perp\times = \begin{bmatrix} 0 & 0 & \partial_y \\ 0 & 0 & -\partial_x \\ -\partial_y & \partial_x & 0 \end{bmatrix} \quad \text{and} \quad J_z = \begin{bmatrix} 0 & -1 & 0 \\ 1 & 0 & 0 \\ 0 & 0 & 0 \end{bmatrix}.$$

By expanding the product $\nabla \times (\mu^{-1}\nabla\times) = (R_\perp + J_z\partial_z)(\mu^{-1}(R_\perp + J_z\partial_z))$, the operators for the vector case are found to be

$$\begin{aligned} Q_1 &= -J_z\mu^{-1}J_z, \\ Q_2 &= R_\perp(\mu^{-1}J_z\,\cdot\,) + J_z\mu^{-1}R_\perp\,\cdot\, = \nabla_\perp \times (\mu^{-1}J_z\,\cdot\,) + J_z\mu^{-1}\nabla_\perp \times\,\cdot, \\ Q_3 &= R_\perp(\mu^{-1}R_\perp\,\cdot\,) = \nabla_\perp \times (\mu^{-1}\nabla_\perp \times\,\cdot\,). \end{aligned}$$

We can now write the electric scalar and vector wave equations in a unified way,

$$(-\mathcal{Q}_1\partial_z^2 + \mathcal{Q}_2\partial_z + \mathcal{Q}_3)\phi = -\mathcal{Q}_4\frac{1}{c^2}\partial_t^2\phi,$$

where $\mathcal{Q}_4 = \varepsilon(x, y, z)$, and we assume for the moment that ε is constant with respect to time. The unknown ϕ represents the electric field, or one of its components.

We recall the moving-time TD-BPM Ansatz (3.5), with E substituted by ϕ,

$$\phi(x, y, z; t) = \mathrm{re}\left(\psi(x, y, z; t)e^{j(\omega_0 t - k_0 n_\mathrm{p} z)}\right).$$

The Ansatz is inserted in the wave equation to derive the TD-BPM equation. This can be done conveniently in terms of the operators

$$\begin{aligned} \mathcal{R}_1 &= jk_0 n_\mathrm{p}, \\ \mathcal{R}_2 &= \frac{1}{c}\partial_t + jk_0. \end{aligned} \tag{3.13}$$

The differential operators ∂_z and $\frac{1}{c}\partial_t$ acting on ϕ relate to operators acting on ψ in the following way

$$\begin{aligned} \partial_z\phi &= \mathrm{re}\left(\rho(\partial_z - \mathcal{R}_1)\psi\right) \\ \frac{1}{c}\partial_t\phi &= \mathrm{re}\left(\rho\mathcal{R}_2\psi\right), \end{aligned} \tag{3.14}$$

where $\rho = e^{j(\omega_0 t - k_0 n_\mathrm{p} z)}$. We can then write the TD-BPM equation for the envelope ψ as

$$-\mathcal{Q}_1\partial_z^2\psi + [2\mathcal{Q}_1\mathcal{R}_1 + \mathcal{Q}_2]\partial_z\psi = [\mathcal{Q}_1\mathcal{R}_1^2 + \mathcal{Q}_2\mathcal{R}_1 - \mathcal{Q}_3 - \mathcal{Q}_4\mathcal{R}_2^2]\psi. \tag{3.15}$$

The final step in the derivation of the moving-time TD-BPM equation is to perform the change of variables (3.8) to the moving time frame. As in the previous section, this is done by substituting ∂_τ for ∂_t and $\partial_\zeta - \frac{n_\mathrm{g}}{c}\partial_\tau$ for ∂_z. However, from (3.14) it follows that we can equivalently write the TD-BPM equation in the moving time variables by substituting ∂_τ for ∂_t, ∂_ζ for ∂_z, and

$$\mathcal{R}_1 = jk_0 n_\mathrm{p} + \frac{n_\mathrm{g}}{c}\partial_\tau \tag{3.16}$$

for $\mathcal{R}_1$ in (3.15). The distinction between fixed and moving time frame can then be made by the choice between (3.13) and (3.16), rather than by the names of the time and longitudinal space variables. In the following we use the variable names z and τ, for easier comparison to literature, when there is no risk of ambiguity.

In summary, (3.15) thus represents the scalar or vector TD-BPM equation, depending on the choice of the $\mathcal{Q}$ operators, and is given in an absolute or moving time frame, depending on the choice of $\mathcal{R}_1$. Further the paraxial approximation is obtained by omitting the first term and the standard BPM equation is obtained by omitting the time dependence of ψ, in which case the $\mathcal{R}$ operators reduce to scalar multiplication factors. The simplified paraxial equation, without the $\partial_\tau\partial_\zeta$ term, is obtained by using, for $\mathcal{R}_1$, (3.13) in the left hand side of (3.15) and (3.16) in the right hand side.

Time-dependent (modulated) permittivity

As discussed in Section 2.1.2, the modulation in an EOM appears as a modification to the right hand side of the wave equation,

$$-\frac{1}{c^2}\partial_t^2(\varepsilon E) = -\frac{\varepsilon_\mathrm{c}}{c^2}\partial_t^2 E - \frac{1}{c^2}\partial_t^2(\delta_\varepsilon E),$$

where $\varepsilon_\mathrm{c} = \varepsilon_\mathrm{c}(x,y,z)$ is the unmodulated permittivity, constant with respect to time, and $\delta_\varepsilon = \delta_\varepsilon(x,y,z;t)$ is the time-dependent shift due to modulation. Since (3.15) is the TD-BPM equation for time-independent permittivity we now let $\mathcal{Q}_4 = \varepsilon_\mathrm{c}$, and add a new term to the TD-BPM equation to represent the shift δ_ε.

The shift is zero outside the active waveguide core, i.e., the part of the core placed between the electrodes guiding the electric signal. Inside the active core δ_ε is assumed to be constant with respect to the transverse directions. It can then be factorized, at given z, as

$$\delta_\varepsilon = \delta_\varepsilon^{\max}\chi_\mathrm{core}(x,y,z)f(z;t),$$

where $\delta_\varepsilon^{\max}$ is the maximal shift, χ_core is the indicator function of the active core (1 inside the active core, 0 otherwise), and f is the normalized co-propagating

modulating signal. The modified TD-BPM equation is

$$-\mathcal{Q}_1\partial_z^2\psi+[2\mathcal{Q}_1\mathcal{R}_1+\mathcal{Q}_2]\partial_z\psi = [\mathcal{Q}_1\mathcal{R}_1^2+\mathcal{Q}_2\mathcal{R}_1-\mathcal{Q}_3-\mathcal{Q}_4\mathcal{R}_2^2]\psi-\mathcal{Q}_5\mathcal{R}_2^2(f\psi), \quad (3.17)$$

where $\mathcal{Q}_5 = \delta_\varepsilon^{\max}\chi_{\text{core}}$.

Chirped initial pulse

Consider the input pulse to the EOM, specified in Section 2.2.2 and illustrated in Figure 2.4(b). It is clear that factoring out the carrier frequency, ω_0, greatly reduces the number of grid points needed to resolve the time dependence of the pulse. However, resolving the chirped pulse still requires a grid which is orders of magnitude finer than for a non-chirped pulse with the same temporal width. One remedy may be to modify the Ansatz (3.5) such as to factor out also the temporal variations due to chirp, as given by the analytically computed propagation of chirped Gaussian pulses in straight waveguides (see, e.g., [7]). This corresponds to a modification of the TD-BPM equation: a linear time dependence is added to the constant terms of the operators $\mathcal{R}_1$ and $\mathcal{R}_2$. The resulting equation is not investigated in this work. For pulses as broad as the EOM input pulse, the effect of the initial chirp on propagation characteristics is expected to be negligible, and the EOM initial data is treated by factoring out the chirp of the input pulse, while neglecting the corresponding modifications of the TD-BPM equation.

3.2.3 Weak formulation

Before stating the weak formulation of (3.17), we need to specify test and trial spaces over the domain $\Omega_\perp \times I_\tau$, where $\Omega_\perp$ is the cross section of the waveguide, truncated by suitable boundary conditions at an artificial boundary $\Gamma_\perp$ at some distance from the core. The interval $I_\tau = [\tau_{\min}, \tau_{\max}]$ for the moving time variable is chosen large enough to cover the non-negligible part of the pulse, such that homogeneous Dirichlet boundary conditions can be used at $\Omega_\perp \times \{\tau_{\min}, \tau_{\max}\}$, without affecting the solution notably.

For the vector equation we take as test and trial spaces

$$\mathcal{W} = \{w \in [L^2(\Omega_\perp \times I_\tau)]^3 : w(\,\cdot\,,\tau) \in \mathcal{V},\ \forall\tau \in I_\tau \text{ and } w(\mathbf{x}_\perp,\,\cdot\,) \in \mathcal{U},\ \forall\mathbf{x}_\perp \in \Omega_\perp\},$$

where for the time dependence it is natural to choose

$$\mathcal{U} = \mathcal{U}(I_\tau) = [H_0^1(I_\tau)]^3.$$

For the transverse space dependence a simple approach would be to use

$$\mathcal{V} = \mathcal{V}(\Omega_\perp) = [H^1(\Omega_\perp)]^3.$$

However, by the continuity condition at an interface between two media (2.8), we know that the component of $\mathbf{E}$ tangential to the interface is continuous, while the

normal component is discontinuous. Under such conditions it is more natural to search for solutions in [35]

$$H(\mathrm{curl}) = \{u \in [L^2(K)]^3 : \nabla \times u \in [L^2(K)]^3\},$$

with $K \subset \mathbb{R}^3$. On the other hand, the domain is in our case restricted to $\Omega_\perp \times \{z\}$ for given z, over which it does not seem natural to consider the three-dimensional curl operator. Further, since we assume the waveguide to be slowly varying with respect to z, the normal vector to the interface between core and cladding is at any point almost normal to z, such that E_z is "almost continuous", by which we mean that it has no, or only small, discontinuities. We can then choose a mixed formulation, with stricter continuity conditions on the longitudinal component, than on the transverse ones:

$$\mathcal{V} = H(\mathrm{curl})(\Omega_\perp) \times H^1(\Omega_\perp),$$

where $H(\mathrm{curl})(\Omega_\perp)$ is a two-dimensional space defined based on a two-dimensional curl operator [36]. This space is a standard choice for finite element formulations of the vector mode problem [9,37], which is solved over $\Omega_\perp$, and where the continuity condition for E_z is fulfilled exactly. It is also frequently used in finite element vector-BPM [38,39], which further motivates its use in the current context.

If PEC conditions are specified on some part of the boundary, say $\Gamma_\perp^1 \times I_\tau$, these are imposed explicitly by choosing (for test and trial spaces)

$$\mathcal{V} = \{u \in H(\mathrm{curl})(\Omega_\perp) \times H^1(\Omega_\perp) : u \times \mathbf{n} = 0 \text{ on } \Gamma_\perp^1 \times I_\tau\}. \tag{3.18}$$

The scalar wave equation is valid for waveguide analysis when the refractive index contrast is small. Then the discontinuity in the normal component of $\mathbf{E}$ at the interface is also small, and all components of $\mathbf{E}$ are "approximately continuous". For the scalar equation we thus choose

$$\mathcal{W} = \{w \in L^2(\Omega_\perp \times I_\tau) : w(\,\cdot\,, \tau) \in \mathcal{V},\ \forall \tau \in I_\tau \text{ and } w(\mathbf{x}_\perp, \,\cdot\,) \in \mathcal{U},\ \forall \mathbf{x}_\perp \in \Omega_\perp\},$$

with $\mathcal{U} = H_0^1(I_\tau)$, and $\mathcal{V} = H^1(\Omega_\perp)$ for homogeneous Neumann boundary conditions at $\Gamma_\perp \times I_\tau$, or $\mathcal{V} = H_0^1(\Omega_\perp)$ for homogeneous Dirichlet conditions.

We are now ready to state the weak formulation of (3.17), assuming homogeneous Dirichlet conditions at $\Omega_\perp \times \{\tau_{\min}, \tau_{\max}\}$. At $\Gamma_\perp \times I_\tau$ we assume PEC conditions in the vector case and homogeneous Dirichlet or Neumann conditions, with $\mathcal{V}$ appropriately chosen, in the scalar case. Note that since we search for complex-valued ψ, the spaces specified above should be taken over $\mathbb{C}$. The weak form is: Find $\psi \in \mathcal{W}$ such that

$$a_{zz}(\partial_z^2 \psi, \chi) + a_z(\partial_z \psi, \chi) + a(\psi, \chi) = 0, \quad \forall \chi \in \mathcal{W}, \quad z > 0, \tag{3.19}$$

where a_{zz}, a_z and a are sesquilinear forms acting on $\mathcal{W} \times \mathcal{W}$, defined in the

following. We let $(\,\cdot\,,\,\cdot\,)$ denote the $L^2(\Omega_\perp \times I_\tau)$ scalar product. Then

$$\begin{aligned} a_{zz}(\,\cdot\,,\,\cdot\,) &= (-\mathcal{Q}_1\,\cdot\,,\,\cdot\,), \\ a_z(\,\cdot\,,\,\cdot\,) &= ([2\mathcal{Q}_1\mathcal{R}_1 + \mathcal{Q}_2]\,\cdot\,,\,\cdot\,), \\ a(\,\cdot\,,\,\cdot\,) &= (\mathcal{Q}_1\mathcal{R}_1\,\cdot\,, \mathcal{R}_1\,\cdot\,) - (\mathcal{Q}_2\mathcal{R}_1\,\cdot\,,\,\cdot\,) + (\mu^{-1}D_\perp\,\cdot\,, D_\perp\,\cdot\,) \\ &\quad - (\mathcal{Q}_4\mathcal{R}_2\,\cdot\,, \mathcal{R}_2\,\cdot\,) - (\mathcal{Q}_5\mathcal{R}_2(f\,\cdot\,), \mathcal{R}_2\,\cdot\,), \end{aligned}$$

where $D_\perp$ represents the transverse gradient, $\nabla_\perp$, in the scalar case, and the "transverse curl", $\nabla_\perp\times$, in the vector case. We have integrated by parts over $\Omega_\perp$ to get

$$(\mathcal{Q}_3\,\cdot\,,\,\cdot\,) = (\mu^{-1}D_\perp\,\cdot\,, D_\perp\,\cdot\,). \tag{3.20}$$

In the scalar case this is standard, and requires no comment. Boundary terms vanish because of the homogeneous (Dirichlet or Neumann) boundary conditions. The integration by parts for the vector case is performed in detail.

Consider the vector identity

$$(\nabla \times \mathbf{b}) \cdot \mathbf{a} = \mathbf{b} \cdot (\nabla \times \mathbf{a}) - \nabla \cdot (\mathbf{a} \times \mathbf{b}). \tag{3.21}$$

Substituting $\nabla_\perp$ for ∇ amounts to disregarding any derivative with respect to z. Hence, by linearity, the same identity must hold for $\nabla_\perp$. The desired integration by parts follows by integrating the identity over $\Omega_\perp$ and applying Green's theorem, a two-dimensional version of the divergence theorem, to the last term:

$$\begin{aligned} \int_{\Omega_\perp} (\nabla_\perp \times \mathbf{b}) \cdot \mathbf{a}\,\mathrm{d}x\,\mathrm{d}y &= \int_{\Omega_\perp} \left(\mathbf{b} \cdot (\nabla_\perp \times \mathbf{a}) - \nabla_\perp \cdot (\mathbf{a} \times \mathbf{b})\right)\,\mathrm{d}x\,\mathrm{d}y \\ &= \int_{\Omega_\perp} \mathbf{b} \cdot (\nabla_\perp \times \mathbf{a})\,\mathrm{d}x\,\mathrm{d}y - \int_{\Gamma_\perp} (\mathbf{a} \times \mathbf{b}) \cdot \mathbf{n}\,\mathrm{d}s, \end{aligned}$$

where $\mathbf{n}$ is a unit vector normal to the boundary $\Gamma_\perp$. Note that because of the asymmetry of the identity (3.21), the integration by parts does not induce a change of sign, as in the scalar case. With $\mathbf{b} = \mu^{-1}\nabla_\perp \times \psi$ and $\mathbf{a} = \chi$ we get

$$(\nabla_\perp\times(\mu^{-1}\nabla_\perp\times\psi), \chi) = (\mu^{-1}\nabla_\perp\times\psi, \nabla_\perp\times\chi) - \int_{I_\tau}\int_{\Gamma_\perp} (\chi\times(\mu^{-1}\nabla_\perp\times\psi)) \cdot \mathbf{n}\,\mathrm{d}s\,\mathrm{d}\tau.$$

By the PEC conditions the test function, χ, is parallel to $\mathbf{n}$ on $\Gamma_\perp$. But then $\chi \times (\mu^{-1}\nabla_\perp \times \psi)$ is orthogonal to $\mathbf{n}$, and the integral over $\Gamma_\perp$ vanishes. We have thereby shown (3.20) in the vector case.

The use of homogeneous Dirichlet or Neumann, or PEC boundary conditions in the derivation is not as restrictive as it may seem. Perfectly matched layers (PMLs), used to avoid reflections from the boundary, correspond to an artificial modification of the material parameters in a layer adjacent to the boundary, but does not impose an actual boundary condition. Boundary conditions must still be chosen for the artificial boundary, but due to the absorbing layer, the solution is not very sensitive to the choice, and homogeneous Dirichlet or Neumann, or PEC conditions may be used.

For the derivation of the weak form (3.19) it was further used that

$$(\mathcal{R}\,\cdot\,,\,\cdot\,) = -(\,\cdot\,,\mathcal{R}\,\cdot\,),$$

for $\mathcal{R} = \mathcal{R}_1, \mathcal{R}_2$. This follows from integration by parts over I_τ, and by noting that the coefficient of the differential term in $\mathcal{R}$ is real, while the constant term is purely imaginary. Boundary terms due to integration by parts vanish because of the homogeneous Dirichlet conditions at $\Omega_\perp \times \{\tau_{\min}, \tau_{\max}\}$.

For the purpose of tensor product finite element discretization, derived in Section 3.2.4, we also note here that for separable functions in $\mathcal{W}$, i.e., for elementary tensors in the tensor product space $\mathcal{V} \otimes \mathcal{U} \subseteq \mathcal{W}$, the sesquilinear forms can be separated as follows

$$\begin{aligned} a_{zz}(\,\cdot\,,\,\cdot\,) &= -(\mathcal{Q}_1\,\cdot\,,\,\cdot\,)_\perp(\,\cdot\,,\,\cdot\,)_\tau, \\ a_z(\,\cdot\,,\,\cdot\,) &= 2(\mathcal{Q}_1\,\cdot\,,\,\cdot\,)_\perp(\mathcal{R}_1\,\cdot\,,\,\cdot\,)_\tau + (\mathcal{Q}_2\,\cdot\,,\,\cdot\,)_\perp(\,\cdot\,,\,\cdot\,)_\tau, \\ a(\,\cdot\,,\,\cdot\,) &= (\mathcal{Q}_1\,\cdot\,,\,\cdot\,)_\perp(\mathcal{R}_1\,\cdot\,,\mathcal{R}_1\,\cdot\,)_\tau - (\mathcal{Q}_2\,\cdot\,,\,\cdot\,)_\perp(\mathcal{R}_1\,\cdot\,,\,\cdot\,)_\tau, \\ &\quad + (\mu^{-1}D_\perp\,\cdot\,,D_\perp\,\cdot\,)_\perp(\,\cdot\,,\,\cdot\,)_\tau, \\ &\quad - (\mathcal{Q}_4\,\cdot\,,\,\cdot\,)_\perp(\mathcal{R}_2\,\cdot\,,\mathcal{R}_2\,\cdot\,)_\tau - (\mathcal{Q}_5\,\cdot\,,\,\cdot\,)_\perp(\mathcal{R}_2(f\,\cdot\,),\mathcal{R}_2\,\cdot\,)_\tau, \end{aligned} \tag{3.22}$$

where $(\,\cdot\,,\,\cdot\,)_\perp$ and $(\,\cdot\,,\,\cdot\,)_\tau$ denote the L^2 scalar products over $\Omega_\perp$ and I_τ respectively.

Stability analysis

We consider stability in a simplified case: the scalar paraxial case with constant permeability, $\mu = 1$, homogeneous Dirichlet boundary conditions and no modulation of the refractive index. Here we mean by the paraxial approximation that both the $\partial_\zeta^2\psi$ and the $\partial_\tau\partial_\zeta\psi$ terms can be neglected. The weak formulation (3.19) then reduces to

$$a_z(\partial_z\psi,\chi) + a(\psi,\chi) = 0, \quad \forall\chi \in H_0^1(\Omega_\perp \times I_\tau), \quad z > 0,$$

where

$$\begin{aligned} a_z(\,\cdot\,,\,\cdot\,) &= 2jk_0n_{\mathrm{p}}(\,\cdot\,,\,\cdot\,), \\ a(\,\cdot\,,\,\cdot\,) &= (\mathcal{R}_1\,\cdot\,,\mathcal{R}_1\,\cdot\,) + (\nabla_\perp\,\cdot\,,\nabla_\perp\,\cdot\,) - (\varepsilon\mathcal{R}_2\,\cdot\,,\mathcal{R}_2\,\cdot\,). \end{aligned}$$

We want to show stability in the sense that $\|\psi(z)\|^2 \leq \|\psi_0\|^2,\ z > 0$, where ψ_0 is the field at $z = 0$. Since

$$\partial_z\|\psi\|^2 = 2\,\mathrm{re}(\partial_z\psi,\psi) = \frac{1}{k_0n_{\mathrm{p}}}\,\mathrm{im}(a_z(\partial_z\psi,\psi)) = -\frac{1}{k_0n_{\mathrm{p}}}\,\mathrm{im}(a(\psi,\psi))$$

it suffices to show that $\mathrm{im}(a(\psi,\psi)) \geq 0$. With the current formulation of the problem this is immediately clear, since

$$a(\psi,\psi) = \|\mathcal{R}_1\psi\|^2 + \|\nabla_\perp\psi\|^2 - \int_{\Omega_\perp} \varepsilon\|\mathcal{R}_2\psi(x,y;\,\cdot\,)\|_\tau^2\,\mathrm{d}\Omega_\perp,$$

where, for real-valued ε, all terms are real, and hence $\mathrm{im}(a(\psi,\psi)) = 0$. In this simplified case the equation is thus not only stable, but also energy conserving.

No rigorous stability analysis has been carried out for more general versions of the TD-BPM equation. It is the impression of the author that no severe stability issues should arise when adding modulated permittivity, because of the perturbative nature of the added term, nor when adding PMLs, since they are constructed to be absorbing, and thus should not increase the energy of the solution. Investigating the stability properties of the vector equation, as well as inclusion of the $\partial_\tau\partial_\zeta$ and ∂_ζ^2 terms, requires more careful considerations.

3.2.4 Discretization

Semi-discrete finite element formulation

While Masoudi *et al.* use finite differences to discretize the moving-time TD-BPM equation in time and transverse space, we formulate here a finite element discretization. This allows for the use of adaptive meshes, and a flexible choice of discrete function spaces. Considering the discussion above on function spaces for the continuous formulation, the latter may be particularly important in the vector case. Furthermore, the geometry, including refractive index discontinuity at the interface between core and cladding, can be represented in an exact manner in the finite element formulation, which is not possible with finite differences.

In a first, straightforward attempt, the entire domain $\Omega_\perp \times I_\tau$ was discretized using a triangular mesh, and the test and trial spaces were defined (identically) as the span of first order continuous Galerkin functions on this mesh. Such an approach has been previously reported in [34], and works well for propagation in waveguides, as long as the solution varies slowly with τ, e.g., the envelope of a pulse with width many times the optical carrier period. However, when refractive index modulation, even with moderate frequency, is added, the solution is blurred along τ. To see why this happens, it is instructive to consider the scalar, paraxial TD-BPM equation in the form (3.11). It is clear that for a propagating mode $\psi = E^0(x,y)$ in a straight waveguide, with no time-dependence other than time-harmonic, the equation reduces to

$$k_0^2(n^2 - n_\mathrm{p}^2)\psi + \Delta_\perp\psi = 0,$$

if n_p is taken to be the effective index of the mode. Since the expression does not involve derivatives with respect to τ, the same relation must hold, theoretically, for $\psi = g(\tau)E^0(x,y)$, for any function g. Consequently, any good discretization $\mathcal{A}^h$ of the operator $\mathcal{A} := (k_0^2(n^2 - n_\mathrm{p}^2) + \Delta_\perp)$ should map $g(\tau)E^0(x,y)$ to zero, or at least satisfy

$$\mathcal{A}^h(gE^0) \approx g\mathcal{A}^h(E^0), \tag{3.23}$$

for arbitrary g.

The discretization of $\mathcal{A}$ with finite differences immediately satisfies the requirement, as it is performed independently at each grid point along I_τ. However,

numerical tests of our initial finite element discretization, based on an unstructured grid over $\Omega_\perp \times I_\tau$, show that the discrete operator applied to $g(\tau)E^0(x,y)$ results in an error term, whose magnitude is proportional to the frequency of g, see Figure 3.2, thus explaining the blurring of the solution when a time-varying modulation is added.

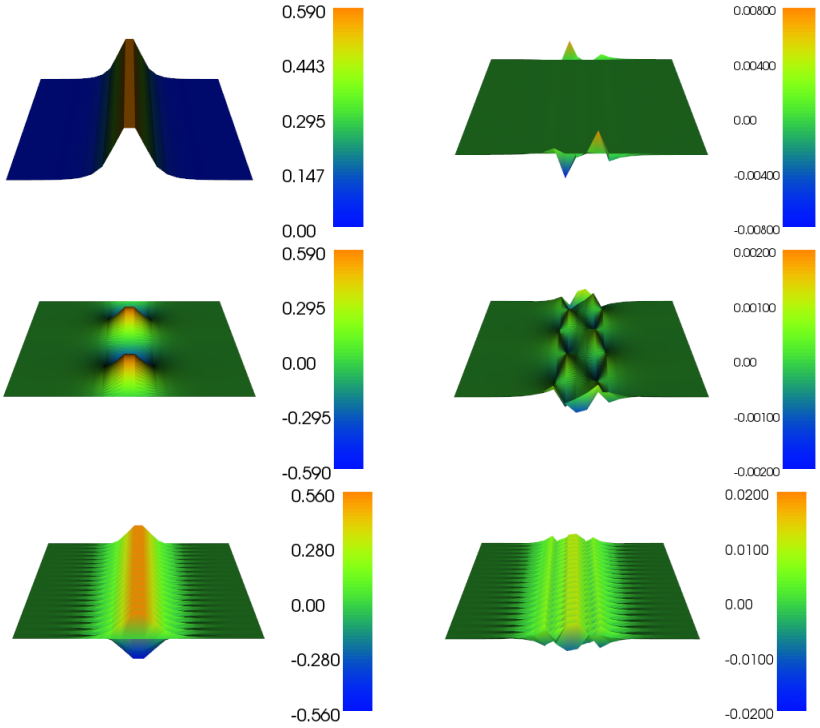

Figure 3.2: Discretization error using finite element discretization with unstructured grid over $\Omega_\perp \times I_\tau$, showing that $\mathcal{A}^h$ does not satisfy (3.23). Left: $\psi = gE^0$, right: $\mathcal{A}^h\psi$. Top: constant g, middle: $g(\tau) = \sin(0.1\tau)$, bottom: $g(\tau) = \sin(\tau)$.

To resolve this issue, we propose to use instead a finite element discretization based on a tensor product space $\mathcal{W}^h = \mathcal{V}^h \otimes \mathcal{U}^h$, where $\mathcal{V}^h$ and $\mathcal{U}^h$ are discrete subspaces of $\mathcal{V}$ and $\mathcal{U}$, respectively. Such an approach is feasible for the TD-BPM equation, since the sesquilinear forms appearing in the weak formulation are separable in the sense of (3.22). Due to this separation of the forms into sums of products of forms acting on $\mathcal{V}^h \times \mathcal{V}^h$ and $\mathcal{U}^h \times \mathcal{U}^h$, respectively, the requirement (3.23) is, as in the case of finite differences, automatically fulfilled.

Tensor product finite elements The finite element formulation of the TD-BPM equation using tensor spaces follows the same structure as that of the boundary value problem in [40, Chapter 16]. The specific choice of finite element subspaces $\mathcal{V}^h$ and $\mathcal{U}^h$ of $\mathcal{V}$ and $\mathcal{U}$, respectively, is discussed at the end of the sec-

tion. For now we consider general such spaces, with $\mathcal{V}^h = \text{Span}\{\phi_j^\perp\}_{j=1}^{n_\perp}$ and $\mathcal{U}^h = \text{Span}\{\phi_j^\tau\}_{j=1}^{n_\tau}$. Note that although the function spaces are over $\mathbb{C}$, real-valued basis functions can be chosen. As the total finite element trial and test space we take the tensor product space $\mathcal{V}^h \otimes \mathcal{U}^h$, with basis functions

$$\boldsymbol{\phi}_\mathbf{j} = \phi_{j_\perp}^\perp \otimes \phi_{j_\tau}^\tau, \quad \text{for } \mathbf{j} = (j_\perp, j_\tau) \in \{1, \dots, n_\perp\} \times \{1, \dots, n_\tau\}.$$

The finite element approximation is thus $\psi^h = \sum_\mathbf{k} \mathbf{x}_\mathbf{k} \boldsymbol{\phi}_\mathbf{k}$, with z-dependent, complex-valued coefficient vector $\mathbf{x}$. Inserting this into the weak form (3.19) results in the semi-discrete TD-BPM equation:

$$\mathbf{A}_{zz}\partial_z^2\mathbf{x} + \mathbf{A}_z\partial_z\mathbf{x} + \mathbf{A}\mathbf{x} = 0,$$

where $\mathbf{A}_{zz}[\mathbf{j}, \mathbf{k}] = a_{zz}(\boldsymbol{\phi}_\mathbf{k}, \boldsymbol{\phi}_\mathbf{j})$, and analogously for $\mathbf{A}_z$ and $\mathbf{A}$. Since the basis functions $\boldsymbol{\phi}_\mathbf{j}$ are elementary tensors, i.e., separable functions of (x, y) and τ, the sesquilinear forms can be written in the factorized form (3.22), and, consequently, the matrices $\mathbf{A}_{zz}$, $\mathbf{A}_z$ and $\mathbf{A}$ can be written as sums of Kronecker products:

$$\begin{aligned}
\mathbf{A}_{zz} &= -\mathbf{Q}_1 \otimes \mathbf{P}_1, \\
\mathbf{A}_z &= 2\mathbf{Q}_1 \otimes \mathbf{P}_2 + \mathbf{Q}_2 \otimes \mathbf{P}_1, \\
\mathbf{A} &= \mathbf{Q}_1 \otimes \mathbf{P}_3 - \mathbf{Q}_2 \otimes \mathbf{P}_2 + \mathbf{Q}_3 \otimes \mathbf{P}_1 - \mathbf{Q}_4 \otimes \mathbf{P}_4 - \mathbf{Q}_5 \otimes \mathbf{P}_5,
\end{aligned}$$

where

$$\begin{aligned}
&\mathbf{Q}_i[j,k] = (\mathcal{Q}_i\phi_k^\perp, \phi_j^\perp)_\perp, \ i \in \{1, \dots, 5\}, && \mathbf{P}_3[j,k] = (\mathcal{R}_1\phi_k^\tau, \mathcal{R}_1\phi_j^\tau)_\tau, \\
&\mathbf{P}_1[j,k] = (\phi_k^\tau, \phi_j^\tau)_\tau, && \mathbf{P}_4[j,k] = (\mathcal{R}_2\phi_k^\tau, \mathcal{R}_2\phi_j^\tau)_\tau, \\
&\mathbf{P}_2[j,k] = (\mathcal{R}_1\phi_k^\tau, \phi_j^\tau)_\tau, && \mathbf{P}_5[j,k] = (\mathcal{R}_2(f\phi_k^\tau), \mathcal{R}_2\phi_j^\tau)_\tau.
\end{aligned}$$

The matrices $\mathbf{Q}_1$, $\mathbf{Q}_4$, and $\mathbf{Q}_5$ are similar to mass matrices, but the integrands include variable coefficients (μ^{-1}, ε_c, and χ_core, respectively), while $\mathbf{Q}_3$ is similar to a stiffness matrix, with integrands depending on μ^{-1}. The matrices $\mathbf{P}_i$, $i = 1, 2, 3, 4$, have integrands with constant coefficients, and can be computed as linear combinations of the standard mass and stiffness matrices, and the matrix with elements of type $(\partial_\tau\phi_k^\tau, \phi_j^\tau)_\tau$, whereas the matrix $\mathbf{P}_5$, representing the shift due to modulation, must be computed as a function of the normalized modulation $f = f(z; \tau)$.

We note here again, that the BPM is obtained as a by-product of the TD-BPM, if the time dependence of ψ is neglected, in which case the $\mathbf{P}$ matrices reduce to scalars. This is convenient from a practical point of view, since it makes it possible to test the implementation of new features concerning the space discretization, such as choice of finite element space or boundary conditions, in frequency domain, before advancing to time domain.

The finite element discretization has been implemented using FEniCS [36], which offers an automated process for matrix assembly, with high flexibility in choice of finite element spaces. The scalar case has been implemented with the

standard first order Lagrange elements ("CG1" in the FEniCS notation) for both time and transverse space dependence, with $\Omega_\perp$ discretized by a triangular mesh. Initial attempts have also been made to implement the vector equation, with CG1 elements for the temporal dependence ($\mathcal{U}^h$). For the transverse spatial dependence, $\mathcal{V}$ is chosen according to (3.18) for the continuous problem, and the discretization is based on the two-dimensional $H(\mathrm{curl})$-conforming Nédélec elements of the first or second kind for the transverse components, and CG1 elements for the z component. Here, of course, the triangulation of $\Omega_\perp$ must be constructed such that interfaces between different media (core and cladding) are aligned with interfaces between triangles.

Perfectly matched layers (PMLs) have been implemented for the scalar case, based on the formulation in [41], developed there for finite element-based BPM.

Discretization in z

We first discretize the weak form of the paraxial TD-BPM equation (with or without the mixed derivative term $\partial_\tau \partial_z \psi$),

$$a_z(\partial_z \psi, \chi) + a(z; \psi, \chi) = 0, \quad \forall \chi \in \mathcal{W}, \quad z > 0,$$

with initial condition $\psi(x, y, 0; \tau) = \psi_0(x, y; \tau)$, in the z direction using the midpoint method. Here we have added one argument to the form a, to indicate that the form may depend on z. The midpoint method, which is an implicit scheme, is stated as:

$$\begin{aligned} &a_z(\psi^n - \psi^{n-1}, \chi) + ka(z^{n-1/2}; \frac{1}{2}(\psi^n + \psi^{n-1}), \chi) = 0, \qquad \forall \chi \in \mathcal{W} \\ &\psi^0 = \psi_0 \end{aligned} \tag{3.24}$$

with step size k, grid points $z^n = nk$, and grid point values $\psi^n = \psi|_{z=z^n}$.

For $a_z(\,\cdot\,,\,\cdot\,) = (\,\cdot\,,\,\cdot\,)$, the midpoint method is unconditionally stable if for all $\psi \in \mathcal{W}$ and at all $z > 0$ it holds that $\mathrm{re}(a(z; \psi, \psi)) \geq 0$. This is shown by setting $\chi = \psi^n + \psi^{n-1}$ in (3.24) and considering the real part of the relation, i.e.,

$$\|\psi^n\|^2 - \|\psi^{n-1}\|^2 = -\,\mathrm{re}\, ka(z^{n-1/2}; \frac{1}{2}(\psi^n + \psi^{n-1}), \psi^n + \psi^{n-1}) \leq 0,$$

where the inequality holds by assumption. In Section 3.2.3 this property was shown for the scalar paraxial case without $\partial_\tau \partial_z \psi$, with homogeneous Dirichlet boundary conditions and without modulation, although there the imaginary, rather than the real part of a was considered, because of the purely imaginary factor appearing in $a_z(\,\cdot\,,\,\cdot\,) = 2jk_0 n_\mathrm{p}(\,\cdot\,,\,\cdot\,)$.

We now combine the finite element discretization for (x, y) and τ with the midpoint method discretization in z to write the fully discretized paraxial TD-BPM equation

$$(\mathbf{A}_z + \frac{1}{2}k\mathbf{A})\mathbf{x}^{(n)} = (\mathbf{A}_z - \frac{1}{2}k\mathbf{A})\mathbf{x}^{(n-1)},$$

where $\mathbf{x}^{(0)}$ is the coefficient vector of the projection of ψ_0 on $\mathcal{W}^h$.

As previously mentioned, Padé approximants have been used in several cases to include second order derivative terms; specifically by Masoudi for a non-paraxial version of the moving-time TD-BPM [31, 32]. In this work, only the paraxial equation is considered, and no attempt has been made to include the second order z derivative term of (3.19).

Chapter 4

Results

4.1 Pulse broadening in straight slab waveguide

In their early work, Masoudi *et al.* [20, 21] use as a test case a straight, symmetric slab waveguide. The accuracy of the TD-BPM is measured in terms of pulse broadening, which can be semi-analytically computed. Here we use that case to compare the performance of the TD-BPM suggested in this work and the FDTD method. We use the scalar paraxial TD-BPM formulation (3.11), and also compare it to the paraxial TD-BPM in [20, 21], where the term $(\frac{n_g}{c})^2\partial_\tau^2\psi$ is neglected.

The considered waveguide has core width 0.5 µm, and refractive index $n_0 = 1.0$ in the cladding, and $n_1 = 1.2$ in the core, at $\lambda_0 = 1.55\,\mu\text{m}$. The shapes and propagation constants – and, hence, effective index, group velocity, and β_2 – of guided modes in a dielectric slab waveguide can be computed numerically, by solving a system of nonlinear equations for two unknowns, as described in Section 2.2.1. In the simulations the waveguide is fed at $z = 0$ with a pulsed first guided TE mode

$$E_y(x, 0, t) = E^0(x)A(0, t)e^{j\omega_0 t}, \tag{4.1}$$

where $E^0(x)$ is the mode shape and $A(0, t) = e^{-t^2/\hat{\tau}_0^2}$ is the Gaussian pulse shape. The propagation of Gaussian pulses in straight waveguides can be described analytically, given the mode shape and propagation constant (as a function of frequency), as discussed in Section 2.2.2. Here we use the half-width at $1/e^2$ intensity point, $\hat{\tau}_0$, rather than the half-width at $1/e$ intensity point, τ_0, used in Section 2.2.2, for a direct comparison with the results in [20, 21], where the pulse width is expressed in $\hat{\tau}_0$. The two half-widths relate as $\hat{\tau}_0 = \sqrt{2}\tau_0$. The pulse broadening is then given by

$$\hat{\tau}_0(z) = \hat{\tau}_0\sqrt{1 + \left(\frac{z}{L_\text{D}}\right)^2}, \tag{4.2}$$

where the dispersion length is defined as $L_\text{D} = \hat{\tau}_0^2/(2|\beta_2|)$. Figure 4.1 shows the theoretical pulse broadening for a few different initial pulse widths, as the pulse propagates a distance of 500 µm through the slab waveguide. Note the different

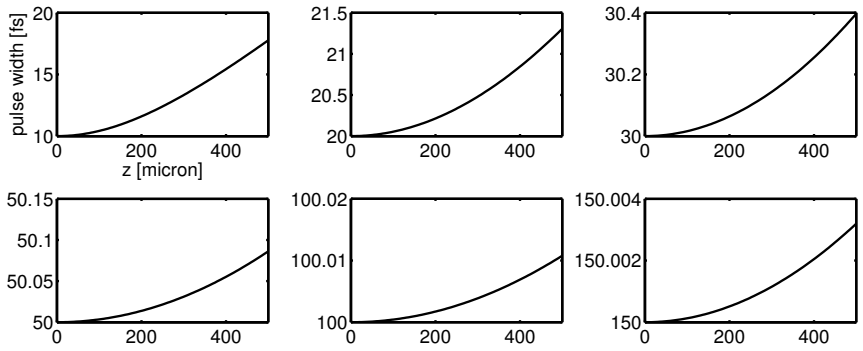

Figure 4.1: Pulse broadening due to dispersion.

scales on the vertical axes; short pulses broaden notably, whereas the longer pulses are almost unaffected by dispersion.

The computational domain for the TD-BPM simulations is $\Omega_\perp = [-X, X]$, with $X = 2.75\,\mu\text{m}$, and $I_\tau = [-T/2, T/2]$, with $T/2 = 2.5\hat{\tau}_0$. Discretization is done with uniform meshes, using $n_x = 110$ elements in the x direction, and $n_\tau = 256$ elements in the τ direction. Corresponding mesh sizes are $h_x = 0.05\,\mu\text{m}$, and $h_\tau = 0.20, 1.0, 2.0$, and $3.0\,\text{fs}$, respectively, for $\hat{\tau}_0 = 10, 50, 100$, and $150\,\text{fs}$. The pulse is propagated from $z = 0$ to $500\,\mu\text{m}$ with step size $h_z = 1.0\,\mu\text{m}$. FDTD simulations are performed with OptiFDTD[1], over the domain $[-X, X] \times [0, Z]$, with X as above, and $Z = 550\,\mu\text{m}$. The initial pulse is specified at an input plane placed at $z = 10\,\mu\text{m}$, and the solution is recorded at "observation points" placed 0, 100, ..., $500\,\mu\text{m}$ from the input plane, along z, and at the center of the waveguide along x. Default mesh sizes are used: $h_x = h_z = 0.083\,\mu\text{m}$, $h_t = 0.19\,\text{fs}$. The final time is chosen such that the peak of the pulse exits the domain with a margin of a few pulse widths. With these mesh sizes, the simulations times for TD-BPM and FDTD are about the same.

In a post-processing step, temporal pulse widths are computed from the simulated data. For TD-BPM, the solution ψ is first integrated against the normalized mode shape E^0, to obtain

$$\psi_{\text{mode}}(z, \tau) = \int_{\Omega_\perp} \psi(x, z, \tau) E^0(x)\, \mathrm{d}x,$$

which is represented in the finite element space $\mathcal{U}^h(I_\tau)$, at given z, by a coefficient vector $\boldsymbol{\psi}$. The center of mass of the pulse is computed using the first moment of ψ_{mode}, and the pulse width is computed using the second moment. The FDTD data is treated similarly, by interpolating the point data to a piecewise linear finite element function on a mesh coinciding with the FDTD grid.

The pulse width as a function of propagation distance, computed using the three different numerical methods, is plotted for initial pulse widths $\hat{\tau}_0 = 10, 50, 100$ and $150\,\text{fs}$, together with the theoretical values in Figure 4.2. It is clear that

[1] 32-bit OptiFDTD (Version 12), © Optiwave, distributed as freeware (www.optiwave.com).

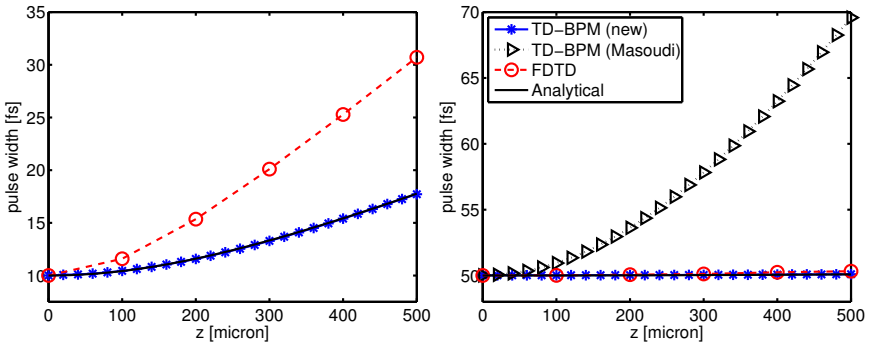

(a) $\hat{\tau}_0 = 10\,\mathrm{fs}$ (b) $\hat{\tau}_0 = 50\,\mathrm{fs}$

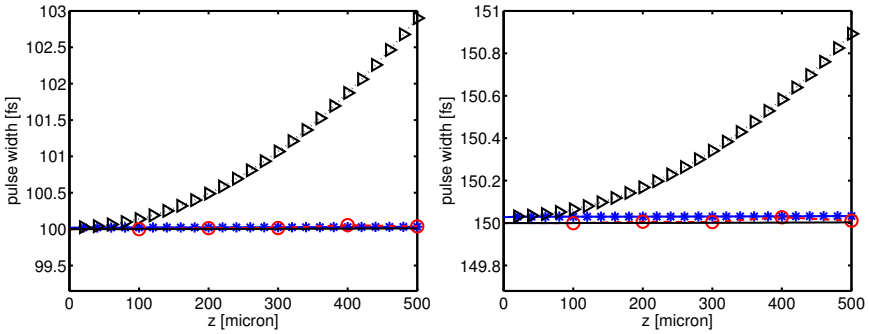

(c) $\hat{\tau}_0 = 100\,\mathrm{fs}$ (d) $\hat{\tau}_0 = 150\,\mathrm{fs}$

Figure 4.2: Simulated pulse width as a function of propagation distance, using FDTD and paraxial TD-BPM with and without the term $(\frac{n_g}{c})^2\partial_\tau^2\psi$.

TD-BPM without the ∂_τ^2 term strongly overestimates the broadening, especially for short pulses (for the shortest pulse, no useful results are obtained with this method). Including the term improves the results dramatically, and the pulse broadening is well approximated in all four cases by the newly proposed paraxial TD-BPM.

The results are summarized in Figure 4.3, in terms of relative pulse width error at $z = 500\,\mu\mathrm{m}$. Note that log-scale is used on the vertical axis. For the TD-BPM by Masoudi *et al.*, the relative error increases from below 1% for $\hat{\tau}_0 = 150\,\mathrm{fs}$ to about 40% for $\hat{\tau}_0 = 50\,\mathrm{fs}$. As previously noted, no useful results are obtained for $\hat{\tau}_0 = 10\,\mathrm{fs}$. With FDTD, the error also increases drastically, from about 0.01% to 70%, as $\hat{\tau}_0$ decreases from 150 fs to 10 fs. With the new TD-BPM, including the ∂_τ^2 term, the error is only about 3% for $\hat{\tau}_0 = 10\,\mathrm{fs}$, and below 0.03% in the other cases. In Figure 4.4 the relative error in pulse width is plotted against propagation distance. Since the relative errors using the TD-BPM method by Masoudi *et al.* can be estimated directly from Figure 4.2, these are excluded in Figure 4.4, to give a better comparison between the new TD-BPM and the FDTD results. The FDTD errors clearly accumulate along z for the short pulses. It is not quite clear

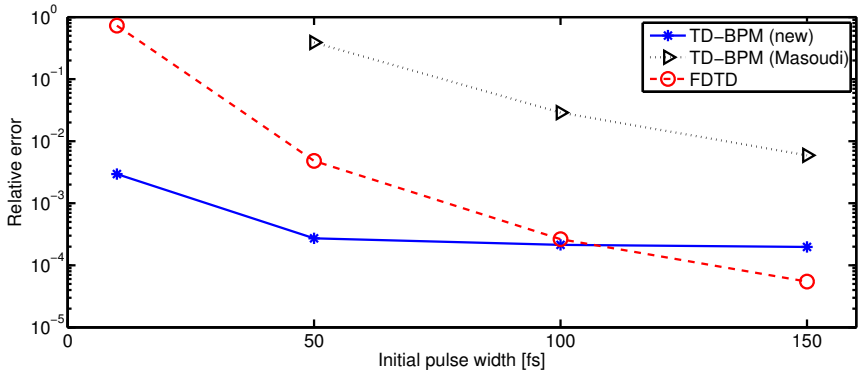

Figure 4.3: Relative error in pulse width at $z = 500\,\mu\text{m}$.

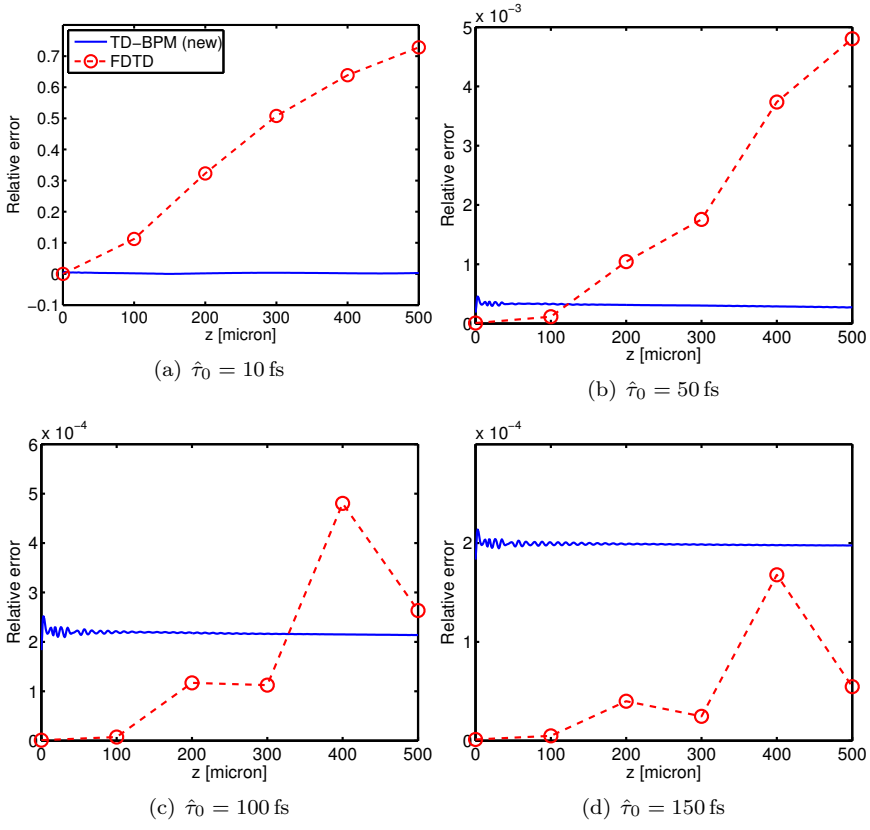

(a) $\hat{\tau}_0 = 10\,\text{fs}$

(b) $\hat{\tau}_0 = 50\,\text{fs}$

(c) $\hat{\tau}_0 = 100\,\text{fs}$

(d) $\hat{\tau}_0 = 150\,\text{fs}$

Figure 4.4: Relative error in pulse width as a function of propagation distance, using FDTD and the newly proposed paraxial TD-BPM (with the term $(\frac{n_\text{g}}{c})^2\partial_\tau^2\psi$). Note that for $\hat{\tau}_0 = 10\,\text{fs}$, the vertical axis starts at a negative value, for the TD-BPM data to be distinguishable from the horizontal axis.

why they fluctuate with z for the longer pulses, however, it may be noted that the fluctuations are small in magnitude. For $\hat{\sigma}_0 = 10\,\text{fs}$, the TD-BPM error does grow with z, but at such a low rate, compared to the FDTD error, that it appears to be constant in the figure. For the longer pulses, the TD-BPM data displays an error even for the known pulse at $z = 0$. This is because the low resolution of the pulse, with 256 mesh cells, limits the attainable precision in the post-process step, in which pulse width is computed. The constant dependence of the error on z indicates that this projection error, rather than the simulation error from TD-BPM, dominates the total error for the longer pulses. This assumption is confirmed by comparing the TD-BPM errors for different resolutions in τ. The case $\hat{\tau}_0 = 100\,\text{fs}$ is shown in Figure 4.5, with $n_\tau = 128$, 256, and 512.

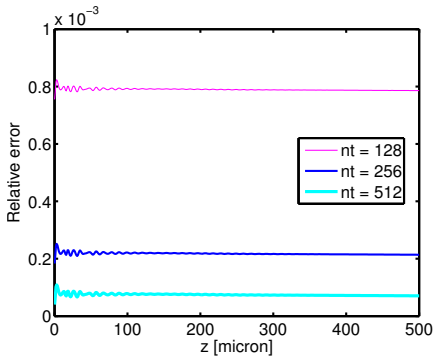

Figure 4.5: Relative error in pulse width as a function of propagation distance, using the newly proposed TD-BPM with varying resolution in τ. Initial pulse width is 100 fs.

It may be noted that with both FDTD and TD-BPM, the total simulated time, T, varies with $\hat{\tau}_0$. However, while the value of $\hat{\tau}_0$ affects T only marginally for FDTD (assuming the propagation distance is large compared to the pulse width), for TD-BPM the two values are proportional. Therefore, as the time step is kept constant for FDTD, the number of time steps also stays approximately constant. To make a fair comparison, the number of time steps (n_τ) for TD-BPM is kept constant, at the cost of making the time step (h_τ) larger with growing $\hat{\tau}_0$. This explains why for TD-BPM, the error does not decrease with increasing $\hat{\tau}_0$, as seen in Figure 4.3. Once the threshold is reached, where the projection error, described above, dominates the error, the total relative error does not decrease with increasing initial pulse width.

The analytical pulse broadening, (4.2), is based on derivations in [7]. It is not obvious that the formula is valid for pulses as short as the ones considered here. However, since the FDTD includes all terms of the wave equation, the consistency between the analytical values and FDTD results indicate that (4.2) is indeed valid for the longer pulses. Also for $\hat{\tau}_0 = 10\,\text{fs}$, FDTD results converge to the analytical prediction as the mesh is refined. However, to reach the same level of accuracy as with the new TD-BPM, the number of grid points along z (and along t, to keep stability) must be increased by a factor four, increasing the simulation time by a

factor 16.

4.2 Electro-optic modulator

As a proof-of-concept case we now consider an EOM with realistic optical input pulse and modulating signal. The geometry is simplified in that a waveguide with one-dimensional cross section, i.e., a slab waveguide, is considered, rather than a rectangular or rib waveguide; more specifically, the cross section and materials are the same as in the previous section. We consider an EOM with Mach-Zehnder geometry, in which the center positions of the waveguide cores are located at

$$x_{\pm} = \begin{cases} 0, & z \in [0, L_1) \cup [L_4, L_{\text{tot}}], \\ \pm\frac{1}{2} W_{\text{bend}}(1 - \cos(\pi \frac{z-L_1}{L_2-L_1})), & z \in [L_1, L_2), \\ \pm W_{\text{bend}}, & z \in [L_2, L_3), \\ \pm\frac{1}{2} W_{\text{bend}}(1 + \cos(\pi \frac{z-L_3}{L_4-L_3})), & z \in [L_3, L_4). \end{cases}$$

Here $L_1 = L_{\text{in}}$, $L_2 = L_1 + L_{\text{bend}}$, $L_3 = L_2 + L_{\text{arm}}$, $L_4 = L_3 + L_{\text{bend}}$, and $L_{\text{tot}} = L_4 + L_{\text{out}}$. The values of the considered EOM are $L_{\text{in}} = 10\,\mu\text{m}$, $L_{\text{bend}} = 120\,\mu\text{m}$, $L_{\text{arm}} = 10000\,\mu\text{m}$, $L_{\text{out}} = 30\,\mu\text{m}$, and $W_{\text{bend}} = 6\,\mu\text{m}$. The geometry is shown in Figure 4.6, with L_{arm} scaled down to $200\,\mu\text{m}$, for illustration purposes.

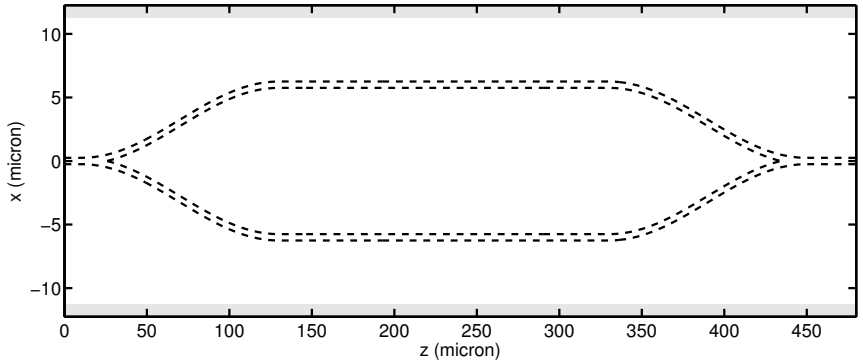

Figure 4.6: EOM geometry. For illustration purposes, the arm length is scaled down by a factor of 50. Gray fields indicate PML layers.

The input pulse is defined as in the previous section by (4.1), with $\hat{\tau}_0 = 877\,\text{ps}$ (i.e., $\tau_0 = 620\,\text{ps}$, as specified in Section 2.2.2). For constant modulation, the accumulated phase shift at the end of the modulated arm is proportional to the permittivity shift,

$$\Delta\phi = \frac{L_{\text{arm}} k_0 C_n}{2 n_{\text{core}}} \delta_\varepsilon, \tag{4.3}$$

where C_n can be computed from the mode parameters of the slab waveguide. For an ideal electric transmission line, with exact velocity match and no electric damping, the permittivity shift δ_ε is constant with respect to z. Then, in the

active arm of the EOM, $\delta_\varepsilon(\tau) = \delta_\varepsilon^{\max} f(\tau)$, where we choose $\delta_\varepsilon^{\max}$, based on (4.3), to be the permittivity shift required for $\Delta\phi = \pi$. A short sequence of Gaussian pulses is taken as modulating signal,

$$f(\tau) = \sum_{k=1}^{3} a_k \exp\left(-\frac{(\tau - \tau_k)^2}{2\tau_{\mathrm{RF}}^2}\right),$$

where the amplitudes, a_k, are 1.0, 0.5, and 0.2, and the offsets, τ_k, are $-5\tau_{\mathrm{RF}}$, 0, and $5\tau_{\mathrm{RF}}$, respectively, for $k = 1, 2, 3$. The half-width is $\tau_{\mathrm{RF}} = \frac{1}{0.2\pi}\mathrm{ps} \approx 1.59\,\mathrm{ps}$, corresponding to spectral half-width (at $1/e$ intensity point) $f_{\mathrm{RF}} = 0.1\,\mathrm{THz}$. The signal is shown as an inset in Figure 4.8.

The transverse computational domain is $\Omega_\perp = [-W, W]$, with $W = W_{\mathrm{bend}} + \frac{1}{2}W_{\mathrm{core}} + W_{\mathrm{clad}}$, where $W_{\mathrm{clad}} = 6\,\mu\mathrm{m}$ is the width of the cladding layer outside the waveguide arms. PML layers with thickness $1\,\mu\mathrm{m}$ are used to truncate $\Omega_\perp$, as indicated by gray fields in Figure 4.6. A homogeneous mesh with mesh size $h_x = 0.0125\,\mu\mathrm{m}$ is used for $\Omega_\perp$. As in the previous section, $I_\tau = [-2.5\hat{\tau}_0, 2.5\hat{\tau}_0]$, which is discretized with a fine mesh size $h_\tau^{\mathrm{fine}} = 0.4\,\mathrm{ps}$ near $\tau = 0$, where the pulse is known to vary rapidly with τ due to modulation. The mesh size is gradually increased to a maximum of 219 ps at the interval edges. A short step size, $h_z = 1.0\,\mu\mathrm{m}$, is used except in the EOM arms, where, after a smooth transition, a step size $h_z = 100\,\mu\mathrm{m}$ is used. We note that such large steps would not be realistic for z-varying modulating signals.

Results are shown in Figure 4.7 as contours of the pulse magnitude over $I_\tau \times \Omega_\perp$ at various propagation distances z along the EOM. The pulse splits equally into the two arms, and amplitude modulation is observed at the center of the pulse as the arms recombine. The simulated amplitude modulation can be more clearly viewed as a function of time by integrating the output field, ψ, against the normalized mode shape, E^0,

$$\psi_{\mathrm{out}}(\tau) = \left| \int_{\Omega_\perp} \psi(x, L_{\mathrm{tot}}, \tau) E^0(x)\,\mathrm{d}x \right|.$$

The theoretical total time-dependent phase shift in the modulated arm is $\Delta\phi(\tau) = \pi f(\tau)$. As a reference for the simulated results we use the magnitude of the sum of two initial pulses, one with and the other without the theoretical phase shift,

$$\psi_{\mathrm{ref}}(\tau) = C_{\mathrm{damp}} \tfrac{1}{2} |1 + \exp(j\Delta\phi(\tau))| A(0, \tau).$$

The damping factor C_{damp}, due to optical losses in the device, is computed by solving the corresponding frequency-domain problem with BPM, and setting $C_{\mathrm{damp}} = \int_{\Omega_\perp} \psi_{\mathrm{BPM}}(x, L_{\mathrm{tot}}) E^0(x)\,\mathrm{d}x$. The simulated results, $\psi_{\mathrm{out}}(\tau)$, are shown along with $\psi_{\mathrm{ref}}(\tau)$ in Figure 4.8 over the full interval I_τ (left), and zoomed in around the modulating signal (right). Excellent agreement between the simulation and reference data can be seen.

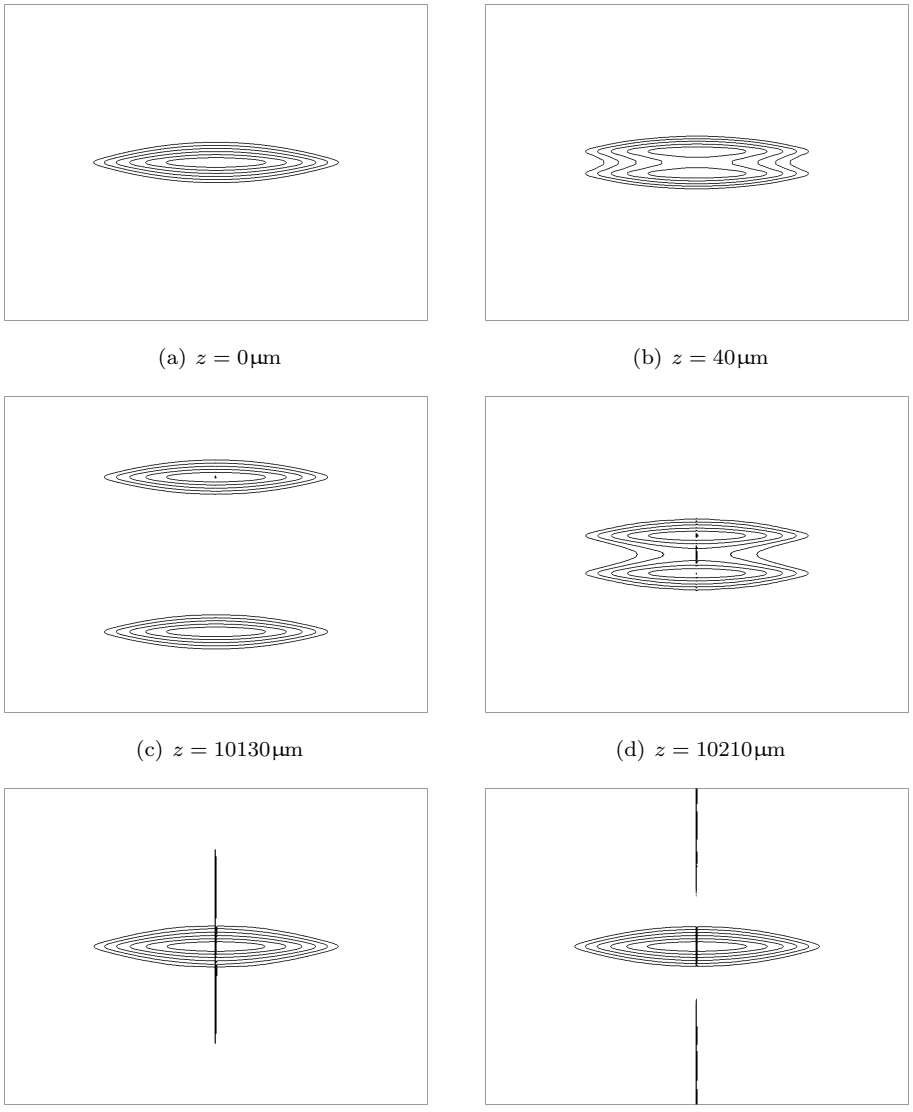

(a) $z = 0\,\mu\text{m}$ (b) $z = 40\,\mu\text{m}$

(c) $z = 10130\,\mu\text{m}$ (d) $z = 10210\,\mu\text{m}$

(e) $z = 10250\,\mu\text{m}$ (f) $z = 10280\,\mu\text{m}$

Figure 4.7: Field distributions for the EOM at different propagation distances z. Horizontal axis: τ, vertical axis: x. Difference between two adjacent contour levels is 3 dB.

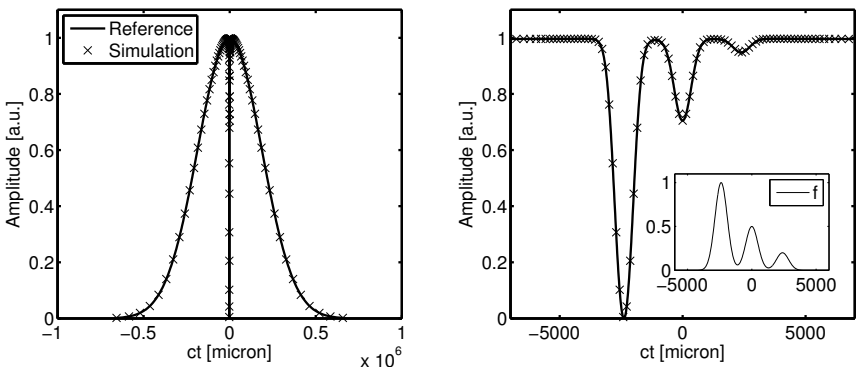

Figure 4.8: Amplitude modulation. Reference: ψ_{ref}, simulation: ψ_{out}. Left: over all of I_τ. Right: zoomed in around the modulating signal. The inset shows the modulating signal $f(\tau)$.

Chapter 5

Conclusion

We have derived weak formulations of the vector and scalar moving-time TD-BPM equations. Based on these, finite element discretizations have been proposed. We have shown that a finite element formulation based on a triangular discretization of the entire domain $\Omega_\perp \times I_\tau$ leads to an erroneous discrete operator for time-dependent solutions, with an error proportional to the frequency of the solution. To achieve a discrete operator without such errors, we proposed to use instead tensor-product finite element spaces. Such a formulation preserves the desired property of finite differences, to separate operators in space and time, while offering the advantages of finite elements in terms of flexible meshes and exact representation of material data at material interfaces. Further, it has been shown, that the accuracy of the paraxial TD-BPM can be significantly improved by a simple modification of the coefficient of the second order time derivative term. The scalar paraxial version has been implemented and validated against analytical data for propagation in a straight slab waveguide. Finally, the method has been applied to an EOM, modulated by a realistic, high-frequency signal.

Reference data for the EOM case were computed by adding the output of two straight arms, one modulated and one non-modulated. The sum was multiplied by a damping factor, computed from a (frequency-domain) BPM analysis of the EOM geometry. The excellent agreement between TD-BPM results and these reference data serves as a mutual validation of the two methods. However, this also indicates, that the assumptions made in the simpler approach used for the reference data are indeed valid, and that using a method for full resolution in space and time, such as the TD-BPM, may not be necessary in this application. For shorter optical pulses, propagating in z-varying structures, a method for space and time resolution is, however, required.

The results presented for the straight waveguide show that the TD-BPM version developed in this work is accurate and efficient, compared to the FDTD method, for short pulses propagating over long distances. In the presented case, the new TD-BPM is 16 times faster than the FDTD method, when computing pulse propagation over 500 µm with the same level of accuracy, for a pulse with

initial width 10 fs. For a device such as the EOM, the propagation distance is about 2 cm, i.e, 40 times longer than the waveguide in the test case. Assuming that the same mesh sizes can be used, the simulation time of TD-BPM scales linearly with the length of the device; the number of steps increases linearly while the time per step remains constant, due to the moving time window. For FDTD, however, the time scales quadratically with device length, since the number of steps and the time per step both increase linearly. This indicates that the TD-BPM may be up to 600 times faster than the FDTD method, with the same accuracy, for ultra-short pulse propagation over 2 cm. We also note that the memory storage required by FDTD increases linearly with device length, while – again due to the moving time window – it is constant for the TD-BPM. Finally we remark that more can be gained from using the new, finite element based TD-BPM, rather than FDTD, when more complex geometries are considered, since it can handle more flexible meshes and thereby avoid the staircasing approximations in FDTD.

A natural and interesting extension to the work presented here would be to consider the non-paraxial TD-BPM. A non-paraxial version based on Padé approximants has been presented by Masoudi *et al.* However, it neglects the second order derivatives $\partial_\tau \partial_\zeta$ and ∂_τ^2, coming from the ∂_z^2 term after change of variables. While the latter term can be included straightforwardly, the former does complicate the formulation. It would also be interesting to implement the vector TD-BPM. However, initial tests indicate that for the vector TD-BPM, as well as when including the mixed derivative term in the scalar paraxial TD-BPM, stability may be a critical issue. Hence, both of these cases require extended stability analyses of the respective equations. Finally, in this work we have considered only non-dispersive materials. Since ultra-short pulses have broad spectra, it would be relevant to extend the method to include dispersive material models.

Bibliography

[1] S. Weber, C. Reinheimer, and G. von Freymann, "Magnification dependent dispersion penalty studied with resonator-based time-stretch oscilloscope," *IEEE/OSA Journal of Lightwave Technology*, vol. 32, no. 20, pp. 3618–3622, 2014.

[2] G. Agrawal, *Lightwave Technology: Components and Devices*. Wiley, 2004.

[3] A. Chen and E. Murphy, *Broadband Optical Modulators: Science, Technology, and Applications*. CRC press, 2011.

[4] K. Okamoto, *Fundamentals of Optical Waveguides*, 2nd ed. Academic Press, 2006.

[5] Z. Pantic and R. Mittra, "Quasi-TEM analysis of microwave transmission lines by the finite-element method," *IEEE Transactions on Microwave Theory and Techniques*, vol. 34, no. 11, pp. 1096 – 1103, Nov. 1986.

[6] D. Cheng, *Field and Wave Electromagnetics*, 2nd ed., ser. Addison-Wesley Series in Electrical Engineering. Addison-Wesley Publishing Company, Inc., 1989.

[7] G. Agrawal, *Nonlinear Fiber Optics*, 3rd ed., ser. Optics and Photonics. Elsevier Science, 2001.

[8] F. Edelvik and B. Strand, "Frequency dispersive materials for 3D hybrid solvers in time domain," *IEEE Transactions on Antennas and Propagation*, vol. 51, no. 6, pp. 1199–1205, Jun. 2003.

[9] J. Jin, *The Finite Element Method in Electromagnetics*, 2nd ed. John Wiley & Sons, 2002.

[10] T. Senior, "Impedance boundary conditions for imperfectly conducting surfaces," *Applied Scientific Research, Section B*, vol. 8, no. 1, pp. 418–436, 1960.

[11] J.-P. Berenger, "A perfectly matched layer for the absorption of electromagnetic waves," *Journal of Computational Physics*, vol. 114, no. 2, pp. 185–200, 1994.

[12] E. Abenius, F. Edelvik, and C. Johansson, "Waveguide truncation using UPML in the finite-element time-domain method," Department of Information Technoogy, Uppsala university, Box 337, SE-751 05 Uppsala, Sweden, Tech. Rep. 2005-026, Sep. 2005.

[13] F. J. Fraile-Peláez, A. Librán, and M. A. Prol, "Spatial effects in the linear propagation of drastically ultrashort optical pulses in single-mode waveguides," *Optical and Quantum Electronics*, vol. 37, no. 7, pp. 611–624, 2005.

[14] G. Gopalakrishnan, W. Burns, R. McElhanon, C. Bulmer, and A. Greenblatt, "Performance and modeling of broadband $LiNbO_3$ traveling wave optical intensity modulators," *IEEE/OSA Journal of Lightwave Technology*, vol. 12, no. 10, pp. 1807–1819, Oct. 1994.

[15] J. Zhou and H. Taylor, "Effect of velocity mismatch and microwave attenuation on time-domain response of traveling-wave electrooptic modulators," *IEEE/OSA Journal of Lightwave Technology*, vol. 18, no. 5, pp. 683–687, May 2000.

[16] M. Tomeh, S. Goasguen, and S. El-Ghazaly, "Time-domain optical response of an electrooptic modulator using FDTD," *IEEE Transactions on Microwave Theory and Techniques*, vol. 49, no. 12, pp. 2276–2281, Dec. 2001.

[17] B. Rahman, V. Haxha, S. Haxha, and K. Grattan, "Design optimization of polymer electrooptic modulators," *IEEE/OSA Journal of Lightwave Technology*, vol. 24, no. 9, pp. 3506–3513, Sep. 2006.

[18] N. Anwar, C. Themistos, B. Rahman, and K. Grattan, "Design considerations for an electrooptic directional coupler modulator," *IEEE/OSA Journal of Lightwave Technology*, vol. 17, no. 4, pp. 598–605, Apr. 1999.

[19] R. Tavlykaev, A. Wiberg, G. Gopalakrishnan, and S. Radic, "Nonlinear distortions in EO phase modulators," *IEEE Photonics Technology Letters*, vol. 24, no. 19, pp. 1778–1780, Oct. 2012.

[20] H. Masoudi, M. AlSunaidi, and J. Arnold, "Time-domain finite-difference beam propagation method," *IEEE Photonics Technology Letters*, vol. 11, no. 10, pp. 1274–1276, Oct. 1999.

[21] H. Masoudi, M. Al-Sunaidi, and J. Arnold, "Efficient time-domain beam-propagation method for modeling integrated optical devices," *IEEE/OSA Journal of Lightwave Technology*, vol. 19, no. 5, pp. 759–771, May 2001.

[22] S. Obayya, *Computational Photonics*. John Wiley & Sons, 2011.

[23] A. Taflove and S. C. Hagness, *Computational Electrodynamics: The Finite-Difference Time-Domain Method*, 3rd ed. Artech House, 2005.

[24] A. Bondeson, T. Rylander, and P. Ingelström, *Computational Electromagnetics*, ser. Texts in Applied Mathematics. Springer, 2005, vol. 51.

[25] R. Chan and J. Liu, "Time-domain wave propagation in optical structures," *IEEE Photonics Technology Letters*, vol. 6, no. 8, pp. 1001–1003, Aug. 1994.

[26] P.-L. Liu, Q. Zhao, and F.-S. Choa, "Slow-wave finite-difference beam propagation method," *IEEE Photonics Technology Letters*, vol. 7, no. 8, pp. 890–892, 1995.

[27] G. Jin, J. Harari, J.-P. Vilcot, and D. Decoster, "An improved time-domain beam propagation method for integrated optics components," *IEEE Photonics Technology Letters*, vol. 9, no. 3, pp. 348–350, Mar. 1997.

[28] M. Koshiba, Y. Tsuji, and M. Hikari, "Time-domain beam propagation method and its application to photonic crystal circuits," *IEEE/OSA Journal of Lightwave Technology*, vol. 18, no. 1, pp. 102–110, Jan. 2000.

[29] T. Fujisawa and M. Koshiba, "Time-domain beam propagation method for nonlinear optical propagation analysis and its application to photonic crystal circuits," *IEEE/OSA Journal of Lightwave Technology*, vol. 22, no. 2, pp. 684–691, Feb. 2004.

[30] J. J. Lim, T. M. Benson, E. C. Larkins, and P. Sewell, "Wideband finite-difference–time-domain beam propagation method," *Microwave and Optical Technology Letters*, vol. 34, no. 4, pp. 243–247, 2002.

[31] H. Masoudi, "A stable time-domain beam propagation method for modeling ultrashort optical pulses," *IEEE Photonics Technology Letters*, vol. 19, no. 10, pp. 786–788, May 2007.

[32] ——, "A novel nonparaxial time-domain beam-propagation method for modeling ultrashort pulses in optical structures," *IEEE/OSA Journal of Lightwave Technology*, vol. 25, no. 10, pp. 3175–3184, Oct. 2007.

[33] H. Masoudi and M. Akond, "Efficient iterative time-domain beam propagation methods for ultra short pulse propagation: Analysis and assessment," *IEEE/OSA Journal of Lightwave Technology*, vol. 29, no. 16, pp. 2475 –2481, Aug. 2011.

[34] L. Bravo-Roger, K. Nóbrega, H. Hernandez-Figueroa, and A. Lopez-Barbero, "Spatio-temporal finite-element propagator for ultrashort optical pulses," *IEEE Photonics Technology Letters*, vol. 16, no. 1, pp. 132–134, 2004.

[35] J.-C. Nédélec, "Mixed finite elements in $\mathbb{R}^3$," *Numerische Mathematik*, vol. 35, no. 3, pp. 315–341, 1980.

[36] A. Logg, K. Mardal, and G. Wells, *Automated Solution of Differential Equations by the Finite Element Method: The FEniCS Book*, ser. Lecture Notes in Computational Science and Engineering. Springer, 2012.

[37] M. Koshiba, S. Maruyama, and E. Hirayama, "A vector finite element method with the high-order mixed-interpolation-type triangular elements for optical waveguiding problems," *IEEE/OSA Journal of Lightwave Technology*, vol. 12, no. 3, pp. 495–502, 1994.

[38] K. Saitoh and M. Koshiba, "Full-vectorial imaginary-distance beam propagation method based on a finite element scheme: application to photonic crystal fibers," *IEEE Journal of Quantum Electronics*, vol. 38, no. 7, pp. 927–933, 2002.

[39] G. D. Ziogos and E. E. Kriezis, "Modeling light propagation in liquid crystal devices with a 3-D full-vector finite-element beam propagation method," *Optical and Quantum Electronics*, vol. 40, no. 10, pp. 733–748, 2008.

[40] W. Hackbusch, *Tensor Spaces and Numerical Tensor Calculus.* Springer, 2012, vol. 42.

[41] Y. Tsuji and M. Koshiba, "Finite element beam propagation method with perfectly matched layer boundary conditions for three-dimensional optical waveguides," *International Journal of Numerical Modelling: Electronic Networks, Devices and Fields*, vol. 13, no. 2-3, pp. 115–126, 2000.